# Investigating Plasmonic Structure-Dependent Light Amplification and Electronic Dynamics Using Advances in Nonlinear Optical Microscopy

Jeremy W. Jarrett, Tian Zhao, Jeffrey S. Johnson, and Kenneth L. Knappenberger, Jr.*

Department of Chemistry and Biochemistry, Florida State University, Tallahassee, Florida 32306-4390, United States

ABSTRACT: Our group has made several recent advances using single-particle nonlinear optical (NLO) microscopy techniques to examine nanostructure-specific plasmon-mediated interactions with electromagnetic energy. These efforts are directed toward the larger goal of optimizing the structure of photonic nanoparticle assemblies for the use and control of energy at the nanoscale. By combining statistical localization methods with second harmonic generation (SHG) imaging, nonlinear signal hot spots can be located within a plasmonic network with nanometer spatial accuracy. This experimental capability was applied to study electromagnetic lensing effects in plasmonic nanoparticle assemblies, with the efficiency of cascaded energy transfer through the network being determined by the resonantly excited plasmon mode. The polarization and time dependencies of the NLO signals were examined using a sequence of phase-locked broad bandwidth femtosecond laser pulses. The methodologies for generating, characterizing, and incorporating these laser pulses into an optical microscope are described. Attosecond control over the temporal separation between two phase-locked laser pulses projected onto orthogonal planes allowed for the generation of a multitude of excitation polarization states; interpulse time delays gave rise to phase shifts ranging from 33 mrad to 2π radians. Left and right circularly polarized light was generated by inducing an interpulse time delay of positive or negative 667 attoseconds (800 nm carrier wave), respectively. These pulse sequences were applied to quantify NLO circular dichroism (CD) signals and to study chiro-optical plasmon amplification in nanostructures predicted to be CD active based on interparticle mode interferences. In order to investigate the time dependence of the NLO responses, plasmon-mediated SHG and two-photon photoluminescence (TPPL) signals were acquired using spectral interferometric detection by projecting both pulse replicas onto a common plane. The SHG signals resulting from plasmon-resonant and nonresonant excitation were analyzed to quantify electronic relaxation rates in metal nanoparticle assemblies. Analysis of TPPL signals revealed structure-specific emission phase shifts reflecting mode-dependent electronic relaxation dynamics. In summary, these results highlight the advantages of NLO imaging with phase-locked femtosecond laser pulses, yielding methodologies for single-structure examination with high spatial accuracy and temporal resolution. NLO signals are inherently plasmon-mode specific, making these methods highly attractive for probing the interplay between nanoscale structure and photonic properties.
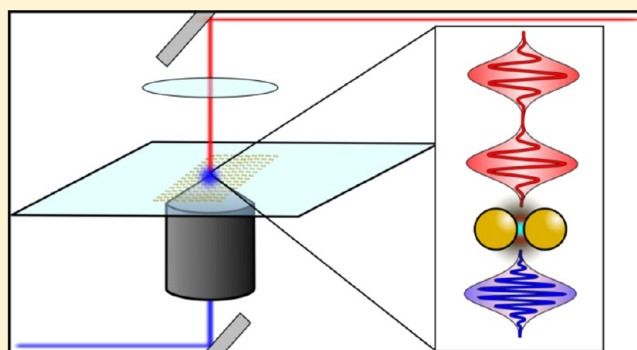
1. INTRODUCTION

Plasmonic nanostructures offer great potential for controlling and using electromagnetic energy on the nanoscale. These opportunities arise from the extraordinarily large electromagnetic absorption and scattering cross sections of these photonic nanoparticles, which, when arranged in close proximity, can transfer and confine energy to specific regions within the nanoparticle network.[1−6] In this way, plasmonic networks can act as efficient optical antennas, whose operational frequencies are determined by the specific nanoparticle arrangement and by material composition. A multitude of nanofabrication techniques have been developed to generate plasmonic nanoparticle assemblies with tailored architectures.[7−27] Describing how these nanoscale structures can be leveraged to control electromagnetic energy is a challenging and active area of physical chemistry and structural plasmonics

research. Hybridization models based on molecular orbital theory have very effectively predicted the steady-state optical properties of coupled metal nanoparticles.[28−36] Similarly, interparticle interference between high-order and dipolar modes can be optimized for selective amplification of specific polarization states of electromagnetic energy.[37−41] By comparison, little is known about time-dependent electron dynamics of nanoparticle assemblies; this information is critical for predictively controlling electromagnetic energy at the nanoscale.

When plasmonic nanoparticles are situated closely enough to allow for strong interparticle electromagnetic coupling, new

plasmon resonances are formed with frequencies that depend on the dielectric and excluded volume separating the nanoparticles.[29,42−44] For cases of interparticle dipolar-mode coupling, the frequency of the newly formed plasmon resonance shifts predictively to lower frequencies with decreasing spatial separation, as explained by the plasmon-ruler relationship.[45−48] This plasmon-ruler model has been used very effectively to measure distances on the nanometer length scale. Interparticle plasmon resonances of hollow, core–shell, and one-dimensional nanostructures are more complex because the nanoparticle building blocks each support multiple plasmon modes that can be hybridized upon electromagnetic coupling. For example, thin-shelled (<5 nm shell thickness) hollow gold nanosphere dimers resonate at higher frequencies than the isolated particles if they are separated by very small distances.[49−52] This unusual frequency increase is attributed to hybridization of cavity plasmon modes that have higher resonance energies than the surface modes of solid structures.[51] However, when neighboring metal nanoparticles are arranged with subnanometer spatial separations that allow for conductive overlap, a charge-transfer type of resonance is formed.[53−55] This charge-transfer plasmon resonance is analogous to an electrical short-circuit that impedes the light amplification typically associated with metal nanoparticles. In contrast to charge-transfer interactions, Fano resonances result when a broad-bandwidth plasmonic antenna interferes with the discrete modes of adjacent nanoparticles.[36,56−63] In the case of nanosphere quadrumers, orientation- (and polarization-) dependent excitation of bright plasmon modes that couple to nanoparticle dark modes and scattering continua exhibit regions of optical transparency.[63] Because coherent interference between short-lived bright and long-lived dark modes is required in order to observe Fano resonances in plasmonic systems, their excitation is expected to modify plasmon-dephasing times. The ability to use nanoparticle arrangement to tailor plasmon decay rates is reflected in the optimization of optical signal amplifications.[36] Fano interference effects have also been observed in time-dependent Raman signals.[64] The wide range of optical phenomena exhibited by electromagnetically coupled plasmonic resonators is providing opportunities for structural control over nanoscale light-matter interactions.

Many advances in understanding plasmonic structure-optical correlations have been made by combining single-particle optical and electron microscopies.[38,39,65−68] Figure 1a portrays a three-dimensional electron tomographic (3D-TET) reconstruction for an aggregate of hollow gold nanospheres with average outer radii of 17 nm and average cavity radii of 13 nm.[52] On the basis of the reconstruction, multiple interfacial structures can be identified, which include spatially separated nanospheres, necked nanoparticles, and, as illustrated by the cross-sectional view shown in Figure 1b, hollow tubular regions. Numerical finite-difference time-domain simulations of the visible-to-near-infrared scattering spectra of nanoparticle dimers based upon interfacial structures recovered from the three-dimensional (3D) TET reconstruction are given in Figure 1 (panels c−f).[52] As Figure 1 data show, the structure of the interparticle gap region plays a large role in determining the optical properties of plasmonic networks. These aspects are critically important because they affect not only the achievable electromagnetic field amplifications but also the operational frequencies of the plasmonic assemblies.[50−52,69,70] These results are but one example emphasizing the importance of examining
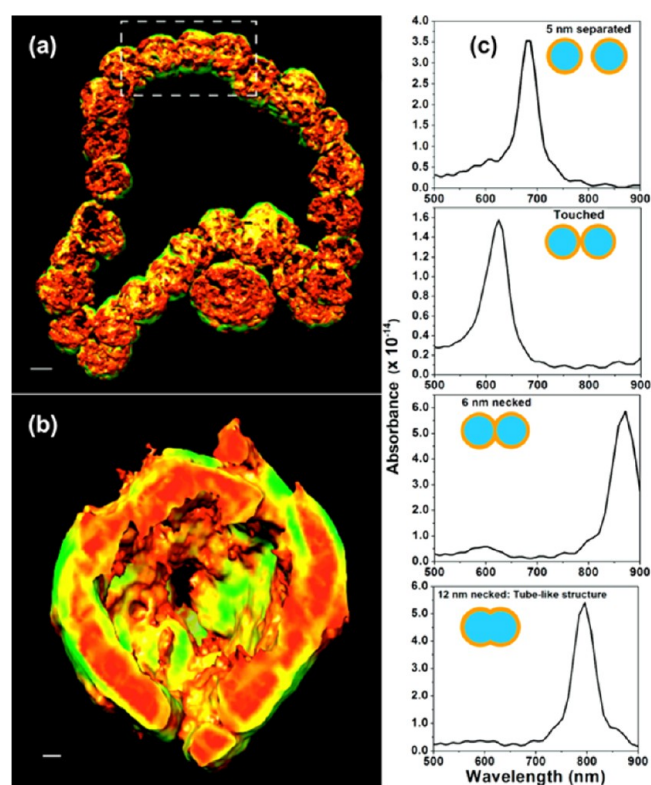

Figure 1. Three-dimensional electron tomographic reconstructions and simulated extinction spectra of aggregated hollow gold nanospheres. (a) Full contour map of reconstructed aggregates, colored by the norm of the gradient of electron microscopy density; scale bar = 20 nm. Red surfaces depict the most rapidly changing densities, whereas blue denotes the slowest change. (b) Rotation by 90° of the region indicated by white box in (a). Scale bar = 3 nm. Numerical analysis of the LSRP frequency for select interparticle structure within the hollow gold nanosphere aggregate: (c) spatially separated hollow nanospheres, (d) dimers formed by a point contact, (e) surface-necked dimer, and (f) hollow tubular-like dimers. The data illustrate the significant impact that seemingly subtle structural changes have on nanoscale optical properties. Adapted from ref 52. Copyright 2011 American Chemical Society.

plasmonic structure-optical correlations at the single-particle level.

An area of plasmonics research that has already benefited significantly from structure−function correlation is surface-enhanced Raman Scattering (SERS).[65,71−77] Through advances in structural imaging technologies, single-molecule-level Raman measurements have been performed on SERS-active substrates.[76,78−82] By extending SERS to include tip-enhanced measurements, the extremely high sensitivity afforded by plasmon amplification has made possible the simultaneous imaging of specific molecular binding sites on colloidal nanoparticles and acquisition of environment-specific vibrational spectra.[73,75] Statistical localization analysis of far-field optical data has also played an important role in understanding plasmon frequency-dependent electromagnetic confinement effects and site-specific catalytic activity.[83−87] Single-particle circular dichroism nonlinear optical measurements also reveal the influence of interfacial structure on chiro-optical signal amplification,[38,41,88] and structure-dependent relative electric and magnetic dipoles of plasmon-mediated optical responses can be quantified using phase-resolved analysis of second harmonic generation (SHG) signals.[39] In these ways, plasmonic

structure-optical correlations are making large impacts in the field of photonic materials design.

Despite substantial progress in optical imaging of single metal nanostructures, only a few groups have developed femtosecond microscopy capabilities appropriate for quantifying electron cooling and plasmon dephasing.[89−104] These measurements are challenging because of the difficulty of spatially and temporally overlapping broad-bandwidth femtosecond laser pulses at the sample plane of an optical microscope. Femtosecond transient absorption microscopy has been an effective tool for examining acoustic damping and electronic relaxation of single nanocubes,[97,98] nanorods,[99] nanowires,[97,102] and nanoplates.[105] Electron dynamics of isolated nanoparticles have also been quantified using femtosecond time-resolved photothermal,[106,107] heterodyne-detected near-degenerate four-wave mixing,[108] and photoelectron imaging.[91,100,101] Few-cycle femtosecond laser pulses have been applied to extract plasmon dephasing dynamics from two-photon photoelectron emission[94] and second harmonic spectral interferometric data.[90,109] Structural influences over plasmon dephasing times are essential to understand for the optimization of photonic properties because electromagnetic signal amplification is directly related to this time constant.[91] Ultrabroad bandwidth few-cycle laser pulse technology is critical for directly probing plasmon coherence effects because the dephasing times of metal nanosystems are typically on the order of tens of femtoseconds.[110−112] Although progress has been made using femtosecond microscopy to study plasmon dynamics, this research has focused primarily on single isolated metal nanoparticles and metal surfaces, leaving a void when it comes to experimental exploration of the plasmon dynamics of electromagnetically coupled nanoparticle assemblies. Application of femtosecond time-resolved single-particle microscopy capable of nanometer spatial accuracy has the potential to fill this need in nanophotonics research by providing both structure-dependent descriptions of electromagnetic energy confinement and interparticle mode-specific electron dynamics.

In this article, we describe some of the recent advances made by our group using single-particle nonlinear optical (NLO) imaging with high spatial accuracy for understanding the influence of nanoscale structure on electromagnetic interactions with nanoparticle assemblies. In particular, we highlight adaptations of broad-bandwidth phase-locked laser pulse replicas to a nonlinear microscope platform for polarization-resolved and femtosecond time-domain imaging. The experimental imaging modes, including the method for generating these pulse replicas and their resultant phase stability, are described in Section 2. Statistical localization methods for determining the position of nonlinear optical signal point sources with nanometer accuracy are described in Section 3a, which also includes examples of how nanoparticle structure can be used for selective confinement of electromagnetic energy to specific regions within a nanoparticle network. In Section 3b, the use of orthogonal phase-locked broad-bandwidth laser pulses for polarization-resolved imaging is described. Section 3c discusses the use of spectral interferometric detection of second harmonic and two-photon photoluminescence (TPPL) signals to examine electron dynamics, including plasmon dephasing, for metal nanoparticle assemblies. The Article is summarized, and prospects for future research directions are given in Section 4.

2. OVERVIEW OF SINGLE-NANOPARTICLE NONLINEAR OPTICAL IMAGING EXPERIMENTAL METHODS

In order to examine nanostructure-specific electromagnetic interactions, we constructed home-built NLO microscopes capable of resolving signals from single plasmonic assemblies.[38,39,41,88,113] Nonlinear optical microscopy is chosen for this purpose because the polarization- and time-dependence of the NLO signals can be used to determine structure-dependent nonlinear susceptibilities and electronic energy relaxation dynamics, respectively. Our imaging systems combine NLO, dark-field, and bright-field scattering capabilities, which allow for accurate determination of nanostructure position within a two-dimensional sample imaging plane. The optical data are correlated to nanoscale structure using electron microscopy.

A schematic of the NLO (SHG-detected) microscope is shown in Figure 2a. The nonlinear optical responses of plasmonic nanostructures are measured using a sample-scanning inverted optical microscope that was built in-house. For the experiments described in this article, either a wavelength tunable or a broad-bandwidth (75 nm bandwidth) mode-locked 80 MHz Ti:sapphire laser was used for excitation. For all experiments, the incident laser power was controllably adjusted using density filters, and the resulting NLO signal intensities were monitored to quantify the order of the nonlinearity. A linear polarizer was placed in the beam path to ensure a high extinction ratio of linearly polarized light. This light was then sent through a pulse replica generator (Sections 3b and 3c data) to control the incident polarization state and interpulse time-delay at the sample plane. The pulse replica generator (Figure 2b) is described below. Pulse replicas were not used for the imaging data described in Section 3a. For experiments relevant to discussion in Section 3a, the laser light was focused to a diffraction-limited spot using a 1.25 NA, 100× oil immersion objective. SHG and TPPL photons were collected by the same objective in epi geometry. For Sections 3b and 3c data, the fundamental was focused to the sample plane using a single aspheric focusing lens (NA = 0.23), and SHG photons were collected in transmission geometry using a 1.25 NA objective. NLO (SHG or TPPL) photons were isolated from laser light using optical filters, focused to the entrance slit of a spectrometer (Shamrock 303, Andor Technology), and directed to a cooled electron-multiplying charge-coupled device (EMCCD) (iXon Ultra 897, Andor Technology). Representative examples of energy-resolved NLO data we obtain using these experimental setups are given in Figure 3. The intensities of signal photons detected at the second harmonic of our laser are plotted versus their detection wavelength in Figure 3a. The log of the integrated intensities of Figure 3a data are plotted versus the log of the incident fundamental wave power in Figure 3b; the slope of two along with the energy-resolved data (Figure 3a) confirm the signal resulted from nanoparticle-mediated second harmonic generation. Typical visible TPPL spectra obtained from single nanostructures at several fundamental laser powers are plotted in Figure 3c. The log of the integrated PL image contrast is plotted versus the log of the incident laser power in Figure 3d, for which a quadratic photon order confirmed the signal was generated by TPPL. The quadratic power dependence of the visible NLO signal was uniform over the entire spectral range examined, as is summarized at the top of Figure 3c. Optical images generated by detection of these NLO signals were
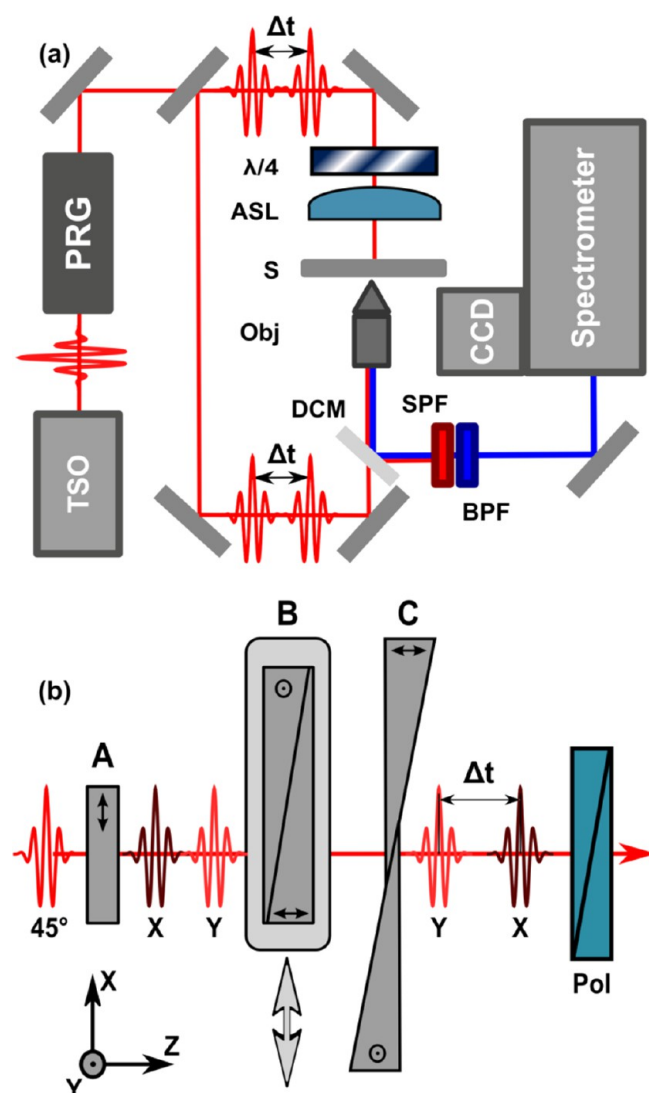
Figure 2. Experimental setup for nonlinear optical imaging (a). Components include titanium:sapphire oscillator (TSO), pulse replica generator (PRG), quarter-wave plate ($\lambda/4$), aspheric lens (ASL), sample (S), 1.25 numerical aperture oil-immersion objective (Obj.), dichroic mirror (DCM), short-pass filter (SPF), band-pass filter (BPF), imaging spectrometer, and electron-multiplying charge-coupled device detector (CCD). Expanded view of the PRG (b), which consists of three distinct α-BBO crystal assemblies (A, B, and C), as described in text, and polarizer.

processed using scripts written in-house. Data analysis methods are described in Section 4.

The setup for dark-field imaging has been described previously.[113] Briefly, a broadband white light source (SPL-2H, Photon Control Inc.) was first polarized using a rotating polarizer and then focused onto the sample with a dry dark-field condenser [Nikon, numerical aperture (NA) = 0.80−0.95] oriented perpendicular to the sample surface. The scattered light from individual dimers was then collected with a 50× air objective (0.75 NA) and both imaged and spectrally analyzed with a spectrometer (Shamrock 303i, Andor Technology) that was coupled to an air-cooled EMCCD (iXon Ultra 897, Andor Technology). The sample was first imaged with a mirror in the light path of the spectrometer to correlate between dark-field and NLO imaging. Once a particle was selected, the mirror was switched to a grating (300 grooves/mm) for spectral analysis.

To collect the spectra, a vertical track of 20 pixels incorporating the dark-field signal was collected as the grating was scanned. An additional track of 20 pixels adjacent to the signal was also collected for background correction. The spectra were corrected by both subtracting and dividing by the background.

Imaging experiments described in Sections 3b and 3c rely on generating NLO signals using a collinear sequence of phase-locked femtosecond laser pulses. The pulse replica generator functions based the translating-wedge-based identical pulses eNcoding system (TWINS), which is inspired by the Babinet-Soleil compensator but adapted to ultrabroadband laser operation.[114,115] Phase-locked, collinearly propagating pulse replicas are generated by a delay line composed of a sequence of α-BBO birefringent crystals cut and assembled into three blocks (A, B, and C), as shown in Figure 2b. This sequence of birefringent materials generates a temporal delay between light polarized along the ordinary and extraordinary axes of block A, which can be controlled with extremely high precision (down to 5.7 attosecond) by transverse translation of the wedges in Block B.

For reference, the input laser source propagates along the z axis and is linearly polarized 45° with respect to the x axis. Block A is a $8 \times 8 \times 2$ mm (xyz) crystal whose optical axis is aligned along the x axis. Block B consists of two wedges, each with dimensions $16 \times 8 \times (0.5-3)$ mm, assembled such that they overlap completely (Figure 2b). One wedge has the optical axis aligned along the y axis and the other along the z axis. This assembly is mounted on a motorized delay stage that translates the position of block B along the laboratory x axis. Block C is composed of wedges identical to those in block B; however, these wedges only overlap by the width of the laser beam.

The laser is first passed through block A, where the incident laser pulse is split into its two orthogonally polarized components, thus forming pulse replicas with a fixed interpulse delay time (Δt) that depends upon the thickness of crystal A (d_A). Next, the pulse replicas pass through block B, affecting only the y-polarized replica. Translating Block B along the x axis temporally displaces the y polarized replica from the x polarized replica in time by changing the thickness of the crystal whose optical axis was oriented along the y axis (d_B). The purpose of block C is to compensate for the angular dispersion introduced by the wedges of block B. The interpulse delay time is a function of the amount of birefringent material inserted, and the refractive indexes of the ordinary and extraordinary axes of the material [$\Delta t = (d_A - d_B)\delta_{eo}$, where $\delta_{eo} = (1/\nu_{ge}) - (1/\nu_{eo})$ and $\nu_{ge}(\nu_{go})$ is the group velocity along the extraordinary (ordinary) axis]. In our experimental setup, the maximum temporal separation between laser pulses was 466.67 fs. However, this interpulse time delay could be doubled to 933.34 fs, at the expense of increasing the minimum step size to 11.4 as. The minimum time step depended upon the precision of the delay stage on which block B moved. The precision of our stage was 0.1 μm, corresponding to a minimum time step of 5.7 attoseconds with our crystal parameters. The induced temporal delays were calibrated using He−Ne interferometric tracking. Since the overall material thickness of the PRG does not change upon translation of block B, the pulse duration of the two replicas does not change.

The phase stability of the pulse replicas is portrayed by the spectal interferogram given in Figure 4. A sequence of high-contrast fringe patterns was obtained by projecting two laser pulse replicas on the same polarization direction using a linear polarizer and maintaining a fixed interpulse time delay. The
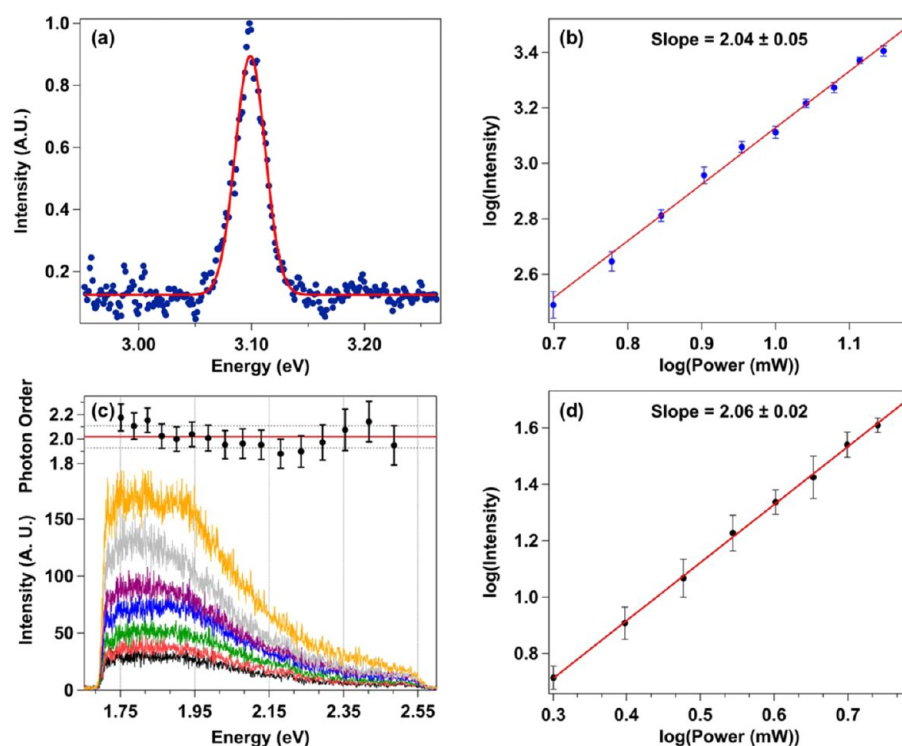
Figure 3. Summary of single-particle nonlinear optical data. (a) Plot of second harmonic generation (SHG) intensity (blue ●) versus detection energy. The red line represents a Gaussian fit to the data. (b) Plot of the log of the measured SHG intensity versus the log of the power of the fundamental wave. The slope of 2.04 ± 0.05 confirms the quadratic power dependence of the SHG signal. (c) Plot of two-photon photoluminescence (TPPL) emission intensity versus emission energy for a single nanoparticle dimer excited at several excitation pulse powers. (d) Plot of the log of the measured global photoluminescence signal (image contrast) vs the log of the excitation pulse power. The slope of 2.06 ± 0.02 confirms the quadratic power dependence of the two-photon photoluminescence response. This nonlinear response was uniform across the entire emission spectrum, as determined by analyzing the power dependence at specific emission energies (c, top).
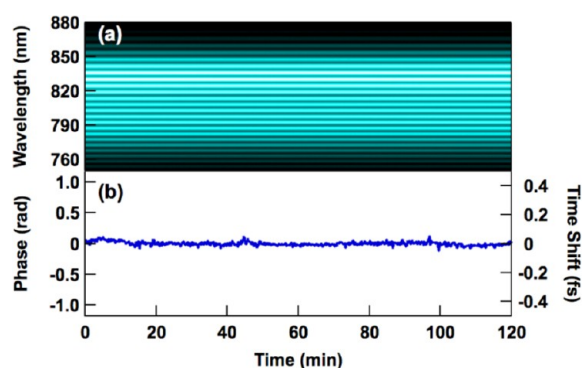

Figure 4. Phase stability of laser pulse replicas. (a) Sequence of fringe patterns acquired while keeping the wedge position fixed for 2 h. (b) Phase fluctuations extracted from (a). The phase jitter was less than 1/190th of an optical cycle. Adapted with permission from ref 116. Copyright 2015 American Institute of Physics.

fringe patterns were recorded over a 2 h period with constant mechanical delay. Figure 4b shows the phase extracted from the measured interferogram acquired over 2 h of data acquisition. The trace shows rms fluctuations of ≈33 mrad, corresponding to delay time fluctuations of ≈14 as or 1/190th of an 800 nm optical cycle. Overall, Figure 4 data provide direct evidence for the persistent phase stability of the pulse replicas we use for nonlinear optical imaging. Further, it is noted that typical image acquisition times are on the order of seconds to minutes. Therefore, the hours-long phase stability afforded by the pulse replicas is more than sufficient for single-particle nonlinear

optical imaging. As is shown in Section 3b, the high phase stability (14 as) and temporal resolution (5.7 as) of our interpulse delays provide us with reliable control over the polarization state of the excitation wave by simply projecting the pulse pairs used to generate the interferogram onto orthogonal planes. This polarization control is used for NLO circular dichroism imaging and continuous polarization variation measurements;[116] the latter imaging mode allows quantification of relative electric and magnetic dipolar contributions for generating image contrast. When the laser pulse replicas are projected on the same plane, spectral interferomeric detection of SHG and TPPL signals allow for examination of plasmon dephasing and electron cooling dynamics, as is demonstrated in Section 3c. The temporal dynamic range of these measurements spans from 0 to ≈940 fs, using ≈10 as time steps.

3a. Electromagnetic Energy Confinement Studied Using SHG Imaging with High Spatial Accuracy. In this section, we describe how diffraction-limited NLO images can be used to determine the electromagnetic energy-confining region of a network with nanometer spatial accuracy. Our localization-based approach to achieving NLO images with nanometer spatial accuracy, which we term nonlinear optical localization using electromagnetic signals (NOLES) imaging, relies on accurately fitting optical data to a two-dimensional Gaussian point-spread function (PSF).[113] Although the image spatial resolution is diffraction limited, the centroid of the PSF can be determined very accurately, pinpointing the center of the signal point source. The factors that typically limit the localization accuracy of experimental images (e.g., noise, drift,
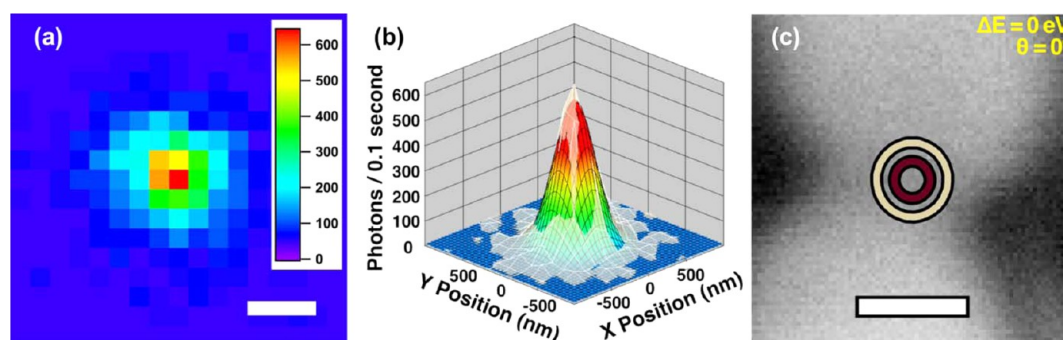
Figure 5. Schematic representation of the nonlinear optical localization using electromagnetic signals (NOLES) imaging technique. (a) A single second harmonic image frame recorded from a gold nanosphere dimer. Scale bar = 500 nm. (b) Overlay of the raw second harmonic image data from (a) with the results from point-spread function fitting (color plot). The imaging rate was 10 frames per second, using a linearly polarized fundamental wave aligned parallel to the dimer interparticle axis. (c) The 1-σ (garnet) and 2-σ (gold) confidence regions for pinpointing the second harmonic point source location overlaid with the respective electron microscopy image. Adapted with permission from ref 113. Copyright 2013 American Institute of Physics.

detector pixel size, etc.) can be overcome by increasing the number of detected signal photons. Although NLO signals are typically weak, plasmonic nanoparticles can function as electromagnetic antennas, increasing optical signal strength and, in turn, the localization accuracy of the image.[113] This antenna effect provides two significant advantages for nano-particle imaging with high spatial accuracy: (1) the accuracy with which the point source position can be determined is significantly increased by plasmon amplification of the NLO signal, and (2) selective excitation of the interparticle plasmon resonance ensures that the image contrast reflects nanostructure mode-specific responses. In the remainder of this section, we describe the NOLES experimental method and demonstrate its capacity for plasmon imaging with high spatial accuracy using nanoparticle dimers as a model system. We also include examples that pinpoint the electromagnetic hot spot using an asymmetric nanoparticle trimer nanolens, for which spatial NLO signal transduction is mode-specific.

To demonstrate plasmon mode-selective imaging, SHG images of single gold nanosphere dimers were recorded at multiple exposure times, fundamental wavelengths, and polar-izations (0° to 360° in 10° steps, where 0° refers to the incident electric field orientation parallel to the dimer axis).[113] For these demonstrations, the nanosphere dimers were formed by benzene dithiol-mediated aggregation, as previously de-scribed.[39] The incident photon flux and the energy bandwidth of the fundamental beam were held constant for all measure-ments described in this section.

For accurate determination of the location of the NLO signal point source originating from plasmon-mediated second harmonic generation, the experimentally acquired two-dimen-sional SHG images were fit using a two-dimensional (2D) Gaussian to construct 3D point spread functions (PSF, Figure 5), which were overlaid with electron microscopy images.[41,113] Specific nanostructures and their NLO responses were then correlated. The indices of the grid pattern on the glass substrate were first determined using bright-field and dark-field imaging in combination with scanning electron microscopy (SEM). By using bright-field imaging for the initial survey, a region of a grid having a specific alpha-numeric index (which provides a fiduciary mark) was selected. Next, the dark-field images and spectra of single gold nanoparticle assemblies located within a specified region were recorded. This spatially addressable spectral determination was repeated at various locations

throughout the sample. SH imaging of specific assemblies was performed by first locating the regions of interest via bright-field imaging. Then, pattern-matching SH signals with the dark-field images allowed the location of specific nanoparticle assemblies. Finally, SH images were recorded while systemati-cally changing the experimental parameters of interest (e.g., fundamental wavelength, polarization state, camera frame rate, etc.). After optical measurements were complete, scanning electron microscopy (SEM) images were used for structural characterization of nanostructures. The indexed grid patterns ensured unique pattern matching between optical and SEM images.

To pinpoint the signal point source, SHG images obtained from single solid gold nanosphere (SGN) dimers were recorded over multiple frames. Figure 5a shows a SHG image (a single still frame of a sequence is shown) obtained from a solid gold nanosphere dimer. In order to quantify the localization accuracy achievable using the sequence of diffraction-limited SHG images, the PSF was first fit to a 2D Gaussian function (Figure 5b):

$$
I(x, y) = z_0 + A \times \exp\left[-\frac{1}{2(1 - cor^2)}\left(\left(\frac{x - x_0}{\sigma_x}\right)^2 \right.\right.
$$
$$
\left.\left. + \left(\frac{y - y_0}{\sigma_y}\right)^2 - \frac{2 \times cor \times (x - x_0)(y - y_0)}{\sigma_x \sigma_y} \right) \right]
$$

(1)

where I is SH intensity, z_0 is an offset in intensity along the z axis, A is an amplitude coefficient, cor is the cross-correlation term, which reflects asymmetry in the PSF (its value lies between −1 and 1; 0 refers to a centro-symmetric image), (x_0, y_0) is the centroid location, and σ_i ($i = x$ or y) represents the x and y standard deviations of the peak.

The accuracy of the center position (x_0, y_0) of the point spread function (PSF) was determined according to eq 2, derived by Thompson et al:[117]

$$
Acc_i = \sqrt{\frac{\sigma_i}{N} + \frac{a^2}{12N} + \frac{8\pi\sigma_i^4 b^2}{a^2 N^2}}
$$

(2)

where Acc_i ($i = x$ or y) is the directional accuracy of the center position of the PSF, σ_i is a result of fitting the signal to the 2D

Gaussian (eq 1), a is the pixel size of the image (in nm), b is the standard deviation of the background (in photons), and N is the number of photons detected.

The number of SH photons detected for each dimer, N, is the sum of photons for all pixels falling under the 2D Gaussian fit. Each frame reported the number of photons detected at the SH wavelength. The signal, in counts, is converted to the number of incident photons detected at the harmonic wavelength according to the following equation:

$$E_V = \left(\frac{cts}{g}\right)\left(\frac{S}{QE}\right)(3.65) \tag{3}$$

where E_V is the total energy of photons, cts is number of counts (per pixel) detected by the EMCCD, g is the amount of electron multiplying (EM) gain applied, S is the CCD sensitivity, QE is the quantum efficiency of the camera in the spectral region of interest, and 3.65 is a physical constant for electron creation in silicon.[118] The number of photons, N, is then determined by dividing the total energy of photons by the energy of a single photon of a specific wavelength of interest.

The image pixel size (a) was calibrated with a TEM grid. The TEM grid was imaged via bright-field imaging with 400 nm light, and the bar width was measured in pixels (244.89 ± 3.49 pixels) and compared to the physical bar width determined by SEM (35.36 ± 0.46 μm). The value for a was 144.37 ± 2.77 nm. To determine b, the standard deviation of the background, a background image was first obtained. Then, using the same pixel locations for determining N, the standard deviation of the background signal (in photons) was calculated. The accuracy values were determined for all successive frames as each experimental parameter was systematically changed (specific wavelength, polarization, exposure time). Average and standard deviations were determined by analyzing multiple frames. The results from the single image (single still frame) displayed in Figure 5c were $\sigma_x = 145.24$ nm, $\sigma_y = 150.95$ nm, $N = 6134$ photons, $b = 1.29$ photons, $Acc_x = 1.93$, $Acc_y = 2.01$ nm.

In a demonstration of mode-selective plasmon imaging, the effects of plasmon amplification on localization accuracies were determined by acquiring SHG images using a range of fundamental wavelengths and polarizations.[113] Figure 6a portrays the importance of matching the fundamental wave and plasmon resonance energies; all data were acquired using equivalent photon fluxes. The localization accuracy is plotted versus the difference between LSPR scattering energy and the energy of the fundamental wave ($\Delta E = E_{LSPR} - E_{fund}$). The optimal localization accuracy results when the plasmon-detuned fundamental energies are minimized; localization accuracies of 3.41 ± 0.28 nm were achieved for resonantly excited nanoparticles using 10 frames per second data acquisition, but detuning the fundamental wave from the LSPR by ≈ 100 meV reduces this accuracy to 16.3 ± 6.5 nm. The localization accuracy was increased to 1.13 ± 0.05 nm by reducing the imaging frame rate to 1 frame per second (Figure 6b). The structural specificity of single-particle SH localization imaging is also reflected in Figure 6a, where results from four different SGN dimer antennas are shown. The different localization accuracies obtained for each structure reflect the sensitivity of the method to interparticle mode coupling.

The mode specificity of SHG localization imaging is further demonstrated using polarization-dependent measurements. For these experiments, the angle formed between the incident fundamental wave and the dimer interparticle axis was altered
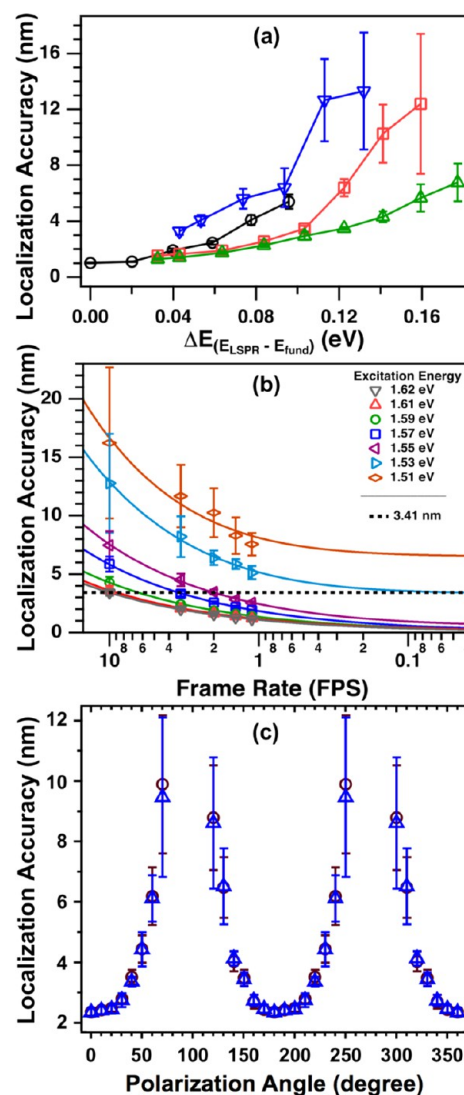

Figure 6. (a) Survey of the localization accuracy achieved from four different nanoparticle dimers, plotted versus the energy difference between the fundamental wave and the LSPR scattering maximum. Large structural dependencies were observed when the fundamental wave was detuned from the LSPR scattering maximum. (b) Summary of localization accuracy dependence on image frame rate and plasmon resonant detuning. (c) Localization accuracy plotted vs the angle formed by the plane of linearly polarized fundamental light and the dimer interparticle axis. Localization accuracies are largest when the plasmon bright mode is excited using linearly polarized light aligned parallel to the dimer axis, and it decreases abruptly as the polarization plane is rotated away from the dimer axis. Taken together, the data demonstrate that mode-specific plasmon resonance imaging with nanometer accuracy can be achieved with high temporal resolution. Adapted with permission from ref 113. Copyright 2013 American Institute of Physics.

using a wave plate/polarizer combination. Excitation of an electromagnetically coupled nanoparticle dimer using light linearly polarized along the interparticle axis generates a bright plasmon mode.[31] Rotation of the light's electric field to the orthogonal axis results in excitation of a dark plasmon mode.[113] SHG localization results obtained by rotation of the incident wave over 360° clearly demonstrates the sensitivity of single-particle imaging to mode selective excitation (Figure 6c).

Next, application of SH localization microscopy for pinpointing the position of the electromagnetic hotspot in a light-harvesting plasmonic nanostructure is described. For this purpose, gold nanoparticle trimers were formed as previously described using directed assembly methods.[88] The asymmetric trimer was chosen as a model system because the judicious arrangement of progressively smaller nanospheres in a linear sequence is expected to result in cascaded focusing of light from the large antenna-like nanoparticle to the junction between the two smallest receiver-like nanoparticles.[6] The effect is demonstrated in the numerically simulated electric field maps in Figure 7a. The simulated data and experimental measure-
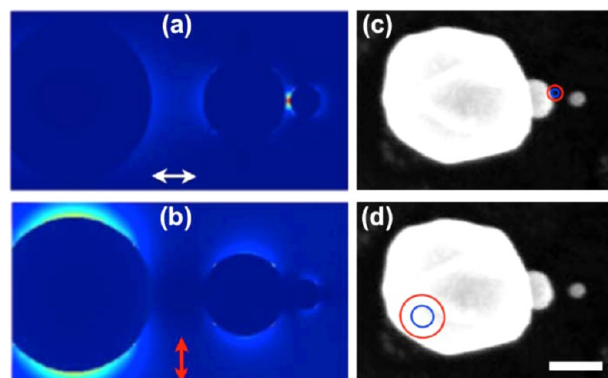

Figure 7. Application of NOLES imaging to determine the polarization-dependent location of nonlinear optical hotspots. Simulated electromagnetic field map for a timer nanolens excited by a fundamental wave aligned (a) parallel and (b) perpendicular to the nanostructure interparticle axis. The dimer consisted of an asymmetric sequence of 250, 80, and 30 nm diameter nanospheres. For (a), incident electromagnetic energy is predicted to be cascaded and localized to the interparticle gap separating the smallest nanospheres. For (b), no energy cascading effect is predicted, and optical signals originate predominantly from the largest of the three nanospheres. Experimental localization using NOLES imaging for (c) parallel and (d) perpendicular fundamental light, reported to 1-σ (blue) and 2-σ (red) confidence levels, overlaid with electron microscopy images of the nanoparticle trimers. The experimental data shown in panels (c and d) confirm the predictions based upon (a and b). The scale bar in (d) represents 100 nm.

ments correspond to a trimer sequence composed of 250, 80, and 30 nm diameter nanospheres. The simulation results shown in Figure 7a indicate that the electromagnetic hotspot is confined between the interparticle gap of the two smallest nanospheres for plasmon-resonant excitation aligned parallel to the trimer axis. In contrast, simulations indicate that excitation orthogonal to the interparticle gap results in the majority of the electromagnetic field being localized to the larger nanosphere (Figure 7b); electromagnetic energy transfer through the nanoparticle network is mode selective.

Experimental localization imaging results are given in Figure 7 (panels c and d). Consistent with numerical predictions, the experimental results confirmed that the electromagnetic energy was localized in the interparticle gap of the two smaller particles (localization accuracy of 7.12 ± 0.65 nm in the x direction and 7.37 ± 0.64 nm in the y direction). As portrayed in Figure 7d, localization imaging indicated that the experimental SHG signal obtained using orthogonal excitation originated from the larger nanoparticle, demonstrating that energy transfer through the network did not occur. The data portrayed in Figure 7 show that nonlinear localization microscopy can be used as a sensitive

tool for examining nanoscale energy transfer and confinement in plasmonic networks. The spatial position of the electromagnetic hot spot within the heterotrimer (Figure 7, panels c and d) was determined to approximately 10-nanometer spatial accuracy by using polarization-corrected localization methods.[119] These spatially distinct hot spots within the trimer that are located using either parallel or perpendicular excitation are separated by less than 100 nm. Therefore, traditional diffraction-limited imaging methods could not have been used to distinguish between these two different responses. By comparison, the high spatial accuracy of the NOLES imaging method makes examination and determination of plasmon mode-selective energy transfer possible. In continuing research, it will be important to determine how structural variations affect electromagnetic nanofocusing efficiency. For example, the spatial separation between nanoparticles, the shapes and number of nanoparticles in an assembly, and their relative orientations are expected to impact the efficiency and distance over which electromagnetic energy can be transported. These structural parameters will also affect interparticle mode-coupling, which determines the resonance frequencies of nanostructures as well as the regions for spatial energy confinement within a nanoparticle network.

3b. Examining Plasmonic Circular Dichroism and Chiro-Optical Amplification in Single Nanostructures Using Orthogonal Phase-Locked Laser Pulses. Another important area for controlling electromagnetic energy on the nanoscale includes understanding the selective interaction of photonic nanoparticles with specific light polarization states. In this section, we describe how the information content of nonlinear optical imaging of plasmonic nanoparticles can be expanded by using phase-locked pulse pairs for excitation. In all of these examples, the nanometer spatial accuracy of the NOLES method is retained, but laser pulse sequencing allows polarization and time-dependent responses to be examined. A major challenge for optical imaging with time-delayed pulses is ensuring their spatial overlap in the focal region of the sample plane. Here, collinear pulse replication circumvents this difficulty because the pulses propagate along identical paths. Before describing data obtained using the laser pulse pairs, we first demonstrate that the spatial accuracy of the images is retained over all pump–probe time delays.

In Figure 8a, the normalized second harmonic intensity is plotted versus interpulse time delay for a single gold nanoparticle heterodimer. Each data point in the interferogram represents the integrated intensity of an imaged SH hot spot taken at the indicated delay time and averaged over three successive time scans. These interferometric data were generated by delaying the two laser pulses relative to each other and measuring the nonlinear response generated by the nanoparticles. The laser pulses were characterized in situ using nonresonant interferometric detection of SHG signals from microscope coverslips processed using in-house programs. Analysis of the SHG data generated by plasmon-resonant nanoparticle excitation was used to determine the spatial stability of our microscope. SH images from individual time points along this interferogram were analyzed using the NOLES technique to determine the spatial stability over the course of a delay scan. Figure 8 (panels b and c) shows the interferometric data overlaid with the x (red) and y (black) relative spatial positions and localization accuracies both near time zero (panel b) and at time delays of approximately +40 fs (panel c). These data show the variation in the measured hot
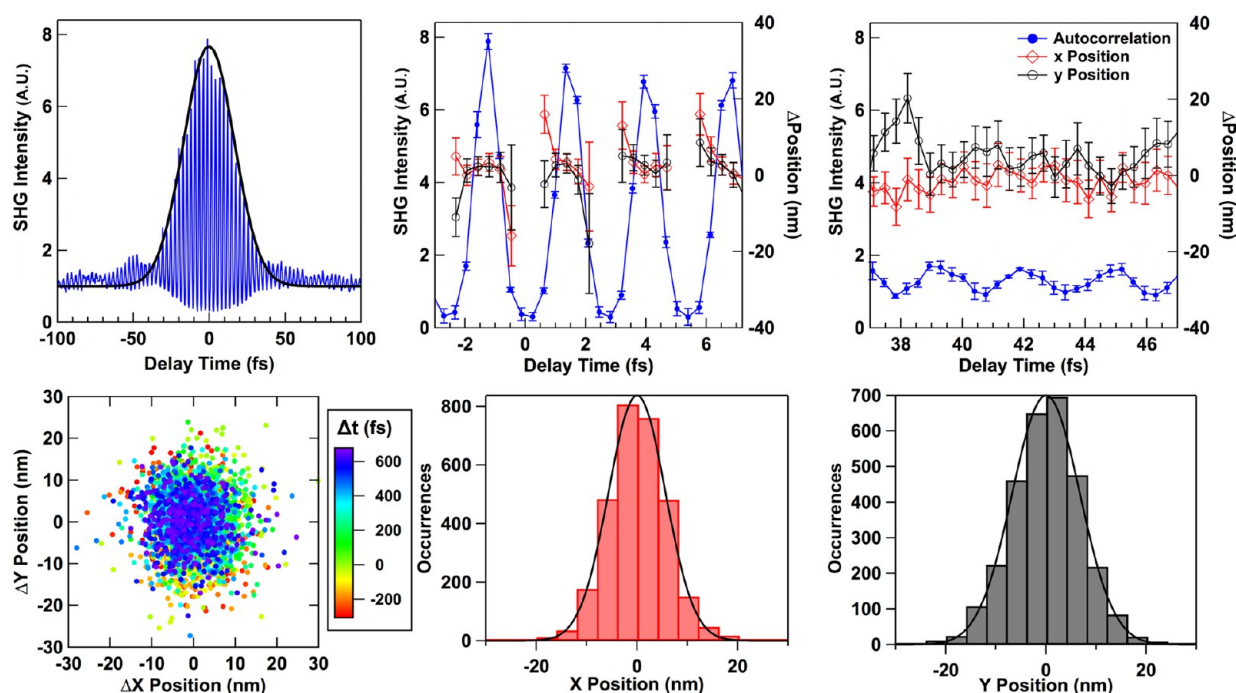
Figure 8. Analysis of the stability of NOLES imaging localization accuracy during the acquisition of femtosecond time-resolved data using collinear phase-locked laser pulses. (a) Second harmonic generation image contrast-detected interferogram, generated using 350 as time steps. The black line represents a Gaussian autocorrelation fit to the interferometric data, (b) comparison of deviations in spatial position (O) and localization accuracy (error bar) determined for different time steps along the first few (<7 fs) interference fringes of the interferogram. (c) Plot for (b) repeated with interpulse time delays of 37−47 fs. (d) Scatter plot comparing all variation in spatial position along both x and y directions obtained over the entire temporal dynamic range of the measurements (−300 fs to +700 fs). Histograms reporting the deviations in spatial positions along the (e) x and (f) y axes over all acquired pump−probe time steps. Both histograms (e and f) were fit to a Gaussian distribution function (overlaid), which revealed the position of the signal point source deviates by less than 10 nm over the course of the femtosecond-time-resolved measurements; these deviations are comparable to the localization accuracies obtained from the NOLES method. Taken together, these data demonstrate the capacity to image single plasmonic nanoparticles with both high temporal (femtosecond) resolution and spatial accuracy (nanometer).

spot location across the time scan. The error bars on the black and red traces represent the $1 − \sigma$ localization values calculated from image analysis. The calculated localization accuracy near the intense peaks at time zero was ~2.5 nm; at delay times near 40 fs, the spatial accuracy was ~5 nm. The reduction in the localization accuracy arose from the reduced SH signal amplitude for longer delay times. Figure 8d shows the measured y position versus x position for all delay times (−300 to +750 fs). A cluster of data points centered around (0,0) was observed. The color scale in the image follows the time delay from −300 (red) to +750 fs (purple). Histograms of the position distribution along x and y are given in Figure 8 (panels e and f). These data were fit to Gaussian functions, yielding standard deviations of $\sigma_x = 5.64 \pm 0.06$ nm and $\sigma_y = 6.74 \pm 0.09$ nm. Taken together, these data demonstrate the spatial localization stability over the experimental time required to acquire femtosecond time-resolved images using our NLO microscope.

As a next step, we have used phase-locked laser pulses for SHG-detected circular dichroism imaging.[116] Our experimental CD imaging setup is depicted in Figure 2a. The excitation source, a mode-locked Ti:sapphire laser (80 MHz, 800 nm center wavelength, 75 nm bandwidth), was circularly polarized using the pulse-replica generator, as described below. After the polarization state was selected, the fundamental wave was focused onto the sample with a single aspheric lens (numerical aperture, NA = 0.23), and the second harmonic (SH) photons generated from the sample were collected in the transmission direction using a 1.25 NA oil immersion objective. SH photons

were then isolated from the fundamental by a series of optical filters and focused to the entrance slit of an imaging spectrometer (Andor Technology, Shamrock 303i) coupled to a cooled EMCCD (Andor Technology, iXon Ultra 897) as described in Section 2.

A depiction of how the phase-stable pulse replicas can be used to generate the circularly polarized excitation source is shown in Figure 9a. In order to generate a circularly polarized
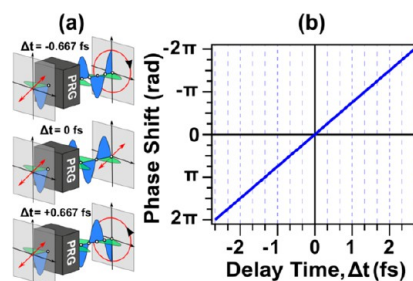

Figure 9. Graphical depiction of how temporally delayed, orthogonal phase-locked laser pulses can be used to generate a multitude of excitation polarization states. (a) Use of the computer-programmed pulse generator to create right (top) or left (bottom) circularly polarized light by inducing an interpulse time delay of ±0.667 fs. Zero time delay produces linearly polarized light. (b) Correlation between the resultant phase shift and the interpulse time delay produced by the pulse replica generator. Adapted with permission from ref 116. Copyright 2015 American Institute of Physics.

fundamental source, the two orthogonal pulse replicas must have an interpulse delay of one-quarter wave ($\pi/2$-phase shift). The PRG can be used to generate these conditions for the 800 nm fundamental by introducing interpulse temporal delays of -0.667, 0, and $+0.667$ fs between phase-locked orthogonal pulse replicas to produce left circular, linear, and right circular polarization states of light, respectively. Figure 9b shows the anticipated phase shift as a function of the delay time between orthogonal pulse pairs. The attosecond delays achievable using the PRG, described in Section 2, allow a multitude of phase shifts to be induced. Here, we demonstrate the generation of horizontally, vertically, elliptically, or circularly polarized output light, depending on the position of block B.

A key feature of the PRG device is its ability to generate pulse replicas that are phase-locked with high stability.[114] The stability of the PRG was characterized by spectral interferometry of ultrashort laser pulses, as described in Section 2. These data showed rms fluctuations of ~33 mrad, corresponding to delay fluctuations of ~14 as or ~1/190th of an optical cycle at 800 nm. The observed phase jitter translated to a 2% fluctuation in the $\pi/2$ phase shift needed to generate circularly polarized light. Overall, these data provided the direct evidence for the long-lived phase stability of the method we use for polarization, or phase, resolved imaging. Combining the phase stability with the delay step precision of 5.7 as, we could reliably produce the polarization states necessary to perform CD imaging, which required interpulse time delays of 667 attoseconds.

Our ability to use pulse replicas to change the excitation polarization state is demonstrated in Figure 10. Figure 10a shows the laser power measured after the PRG as the interpulse delay time was varied, and the output was analyzed using a linear polarizer, graphically depicting the accessible polarization states for interpulse time delays spanning from -1.33 fs to $+1.33$ fs sampled at 30 as intervals. This delay range corresponded to a π phase shift between the two pulses in both time directions (1/2-wave rotation). Figure 10b depicts slices of the data from Figure 10a at time delays of 0, $+0.40$, and $+0.67$ fs, which correspond to linear, elliptical, and circular polarization states. The black trace, taken at 0 time delay, showed a dipolar pattern and corresponded to linearly polarized light. The light blue trace represents data obtained using a $+0.40$ fs interpulse time delay; it has more intensity in the orthogonal direction than the black trace, reflective of an elliptical polarization state. The red trace shows no change in measured laser power, regardless of the analyzer rotation angle, and it thus depicts circular polarization. By precompensating for frequency-dependent dispersion induced by the optics, we were able to ensure the degree of circular polarization was uniform across the entire spectral bandwidth of the laser pulses.[116] In Figure 10c, we show data collected at -1.33 (black), -1.06 (blue), and -0.67 (green) fs time delays. Generation of a -1.33 fs time delay between two orthogonal phase-stable 800 nm pulse pairs is equivalent to inducing a 1/2-wave (π-phase shift) rotation with respect to the pulse pair at zero time delay. The black trace in Figure 10c depicts a linear polarization state, oriented orthogonal to the dipolar pattern obtained using zero interpulse time delay (Figure 10b; black trace). These experimental results confirmed predictions based on the interpulse time delay. The blue trace was generated using an interpulse time delay of -1.06 fs. Under this condition, the fundamental wave was elliptically polarized with the major axis of the ellipse along the x axis (i.e., orthogonal to the blue trace
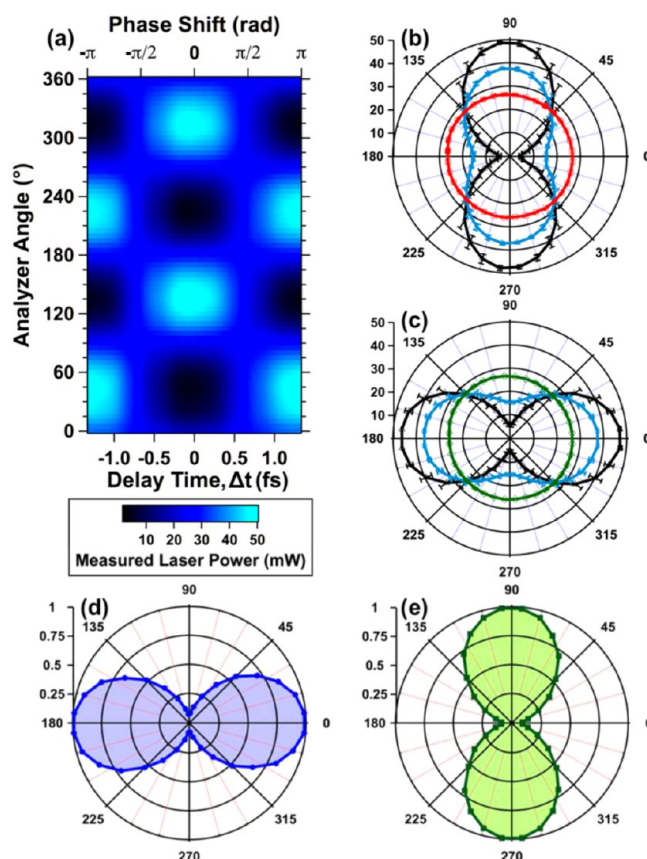

Figure 10. (a) Colormap of measured output power from pulse replica generator with respect to linear polarizer analyzer angle and interpulse delay time. (b) Vertical slices from (a) along delay times of 0 fs (black), $+0.40$ fs (blue), and $+0.67$ fs (red). (c) Slices along delay times of -1.33 fs (black), -1.06 fs (blue), and -0.67 fs (green). (d) RCP and (e) LCP light generated at $+0.67$ and -0.67 fs analyzed with a QWP/LP set. Orthogonal orientation confirmed that LCP and RCP light is generated. Adapted with permission from ref 116. Copyright 2015 American Institute of Physics.

in Figure 10b). The green trace portrays the measured laser power generated at an interpulse delay of -0.67 fs, corresponding to a $\pi/2$ phase shift and generating a circularly polarized fundamental wave. Taken together, these data demonstrated that controlling the interpulse delay between two orthogonal phase-locked laser pulses allowed the PRG device to function as an efficient variable wave plate.

We analyzed the circularly polarized PRG-produced light with a quarter-wave plate/linear polarizer (QWP/LP) combination to ensure that both left- and right-handed polarization states were generated. The QWP transformed the circularly polarized light back into linearly polarized light, and the polarization angle was measured with a linear polarizer. We first translated the block B motor to -0.67 fs to produce circularly polarized light. Then, we analyzed this light with the QWP/LP combination and observed a dipolar pattern with the major axis aligned along the x axis at 0° (Figure 10d). This confirmed circular polarization of the light, and we denoted this light as left circularly polarized (LCP). Then, keeping the quarter-wave plate fixed, we translated the motor to $+0.67$ fs and measured the laser power as the linear polarizer was rotated. We again observed a dipolar intensity pattern but with the major axis along the y axis at 90° (Figure 10e). These results indicated a different handedness to the polarized light (i.e., polarization

state), and we denoted this configuration as right circularly polarized (RCP). Taken together, these data demonstrated our ability to produce light of many polarization states, specifically the LCP and RCP necessary for CD imaging.

To demonstrate the effectiveness of the pulse replicas for CD imaging, the LCP and RCP light generated from the PRG was used to perform SHG-detected CD imaging on plasmonic gold nanoparticle (GNP) dimers.[88] GNP heterodimers were chosen for this demonstration because they exhibit nonzero CD owing to a combination of interfacial chirality and interparticle dipolar and multipolar interference.[38,120−122] SEM images of the heterodimer and homodimer nanoparticle systems are displayed in Figure 11, along with finite-difference time-domain
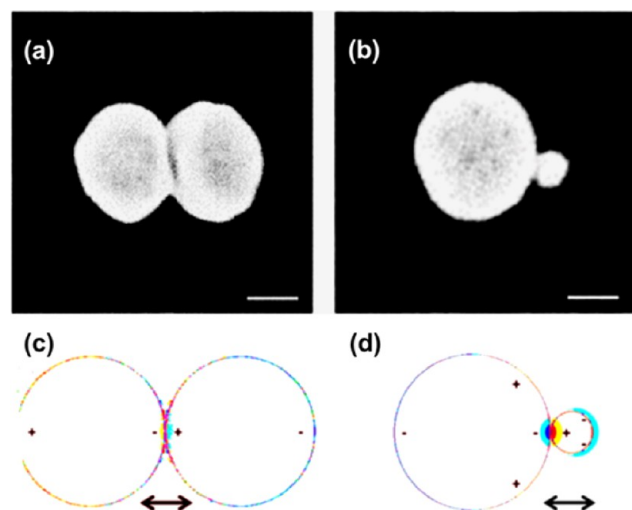

Figure 11. Scanning electron microscope images for the (a) homo and (b) heterodimer nanostructures examined in Section 3c. Scale bars represent 75 nm. Numerical simulations (finite-difference time-domain) of the resonant plasmon mode structures for the (c) homo- and (d) heterodimers. The homodimer system is excited by dipolar−dipolar interparticle coupling. The heterodimer is excited by interference between higher-order modes, which are expected to result in circular dichroism. Adapted from ref 88. Copyright 2015 American Chemical Society.

simulations of their interparticle mode structures.[88] The homodimer system contained two gold metal nanoparticles with 150 nm diameters separated by a 1−10 nm gap (Figure 11a), and the heterodimer system consisted of two gold MNPs with 150 and 50 nm diameters separated by a 1−10 nm gap (Figure 11b). Sample preparation and characterization details have been reported previously.[88] For the homodimer, the interparticle resonance is predicted to result from dipole−dipole plasmon coupling (Figure 11c). In contrast, the heterodimer excitation involved interference between higher-order modes, which is expected to induce circular dichroism (Figure 11d).

Differential CD is reported as a normalized quantity known as the SHG circular difference ratio (SHG-CDR) given by eq 5:[37]

$$|SHG - CDR| = \left| \frac{2(I_{2\omega}^{LCP} - I_{2\omega}^{RCP})}{(I_{2\omega}^{LCP} + I_{2\omega}^{RCP})} \right|$$

(5)

where $I_{2\omega}$ is the number of SHG photons imaged with LCP and RCP excitation. Figure 12 shows the SHG-CDR from gold nanoparticle assemblies. A large, unambiguous difference in
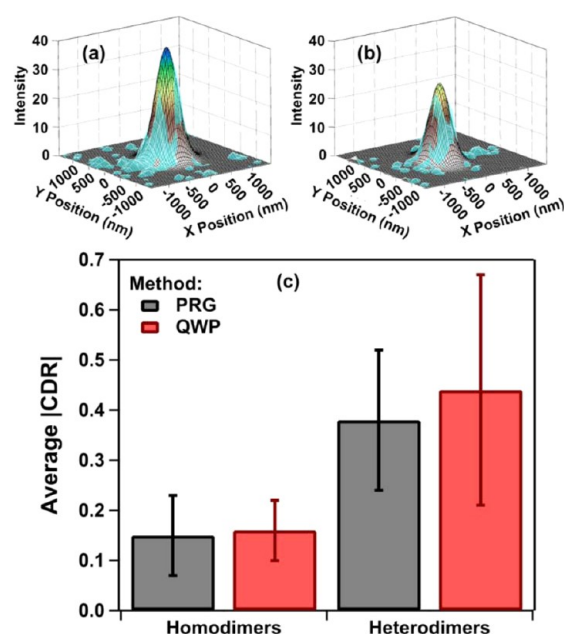

Figure 12. (a,b) SHG data generated from (a) LCP and (b) RCP excitation. (c) Comparison of average SHG-CDR values obtained for two different nanoparticle systems generated from two different methods, QWP and PRG. Adapted with permission from ref 116. Copyright 2015 American Institute of Physics.

intensity was observed upon excitation with LCP versus RCP (Figure 12, panels a and b). The corresponding SHG-CDR for this nanostructure was calculated as 0.35. The total acquisition time for CD images included both the required exposure time and the time needed to switch between LCP and RCP excitation. Computer control of the PRG allows for rapid changing of the polarization state without manual optic manipulation (e.g., wave plate rotation), thus reducing the image acquisition time by a factor of 3. Furthermore, rapid transformation of the fundamental polarization between LCP, RCP, and linear polarization states as well as construction of image statistics for individual particles was obtained via computer programming. As a result, the reproducibility of the measurements could be analyzed by sampling polarization states in an arbitrary sequence.

To test PRG performance, we measured the average SHG-CDR of two different GNP systems and compared the results obtained using both the PRG and a QWP for generation of left and right circularly polarized excitation. Data were compared for 5 different heterodimer samples and 12 different homodimer samples using QWP and PRG for excitation (Figure 12c). For the heterodimers, the QWP method produced an average SHG-CDR value of 0.44 ± 0.23, and the PRG method produced an average value of 0.38 ± 0.16. For the homodimers, the average values were 0.16 ± 0.06 (QWP) and 0.15 ± 0.08 (PRG). Nonzero SHG-CDR values for homodimers were attributed to the asymmetric interfacial structure formed by the inherent heterogeneity of gold nanospheres. The results from these two independent methods were within error of each other, showing the PRG to be a viable means to produce the excitation source necessary for CD imaging. Moreover, the short acquisition times and ease of transforming the laser polarization state allow for rapid CD imaging and single-particle spectroscopy.

Focusing broadband and circularly polarized light using multielement lenses can lead to detrimental achromatic and phase distortions that render CD data unreliable. We also found that light reflection by the dichroic mirror used in our imaging setup changed the polarization state from circular to elliptical. Using the PRG, we precompensated for this shift by changing the time delay between pulses to achieve circular polarization states after the dichroic mirror. However, when performing CD imaging experiments using circularly polarized light generated in this manner in conjunction with a high-numerical aperture objective, the average CD values obtained for well-characterized nanostructures did not agree with known CDR values. This indicated that the compound objective caused an inherent phase shift of the fundamental that could not be corrected using the PRG alone, and CD imaging carried out in the epi-collection geometry was not reliable. For this reason, we performed SHG-CDR experiments operating in transmission geometry to avoid unfavorable phase shifts induced by the dichroic mirrors and multielement compound objectives used in epi-collection microscopes.

Phase-locked orthogonal pulse replication provides a novel and simple way to produce reliable circularly polarized excitation for CD imaging applications. We demonstrated that controlling the temporal delay between orthogonal phase-locked pulse pairs could be used to change the polarization state of excitation and fundamental light, providing user control over the phase relationship of the pulse replicas. Using our setup, phase shifts of as little as 33 mrad are possible, as are 2π phase shifts. As we demonstrated, controlling the interpulse time delay of the pulse pairs proved as effective as a functional wave plate for generating many different excitation polarization states. Significant advantages of the pulse replica method over wave plates include programmed control over the interpulse delays, rapid and high through-put image acquisition, and artifact-free polarization manipulation over 2π radians. We expect that the use of phase-locked pulse replicas for polarization-resolved optical imaging will find widespread use in many nonlinear optical imaging applications, particularly in nanoplasmonics.

The information content that can be obtained using a sequence of orthogonal phase-locked laser pulses can be extended by acquiring images over the full functional range of pump−probe time delays (i.e., phase shifts). For example, the relative electric and magnetic dipolar contributions to nonlinear optical data can be determined for many SHG-active samples by the method of continuous polarization variation (CPV).[37,123] Here, we demonstrate this capability using both symmetric and asymmetric plasmonic bowtie nanostructures.[41] For the CPV experiments, the SH intensity is typically recorded as the polarization state of the fundamental wave is continuously changed using a rotating QWP.[123] However, these phase shifts can be much more effectively sampled by scanning the interpulse time delay of the orthogonal replicas. Analysis of the resultant SHG-CPV line shape allows for quantification of the relative electric- and magnetic-dipolar contributions to the nonlinear response. In general, SHG originates from P, an induced nonlinear polarization at the fundamental frequency, and M, a magnetization component at the harmonic frequency, expressed as[37]

$$P_i(2\omega) = \sum_{j,k} \chi_{ijk}^{eee}(2\omega, \omega, \omega)E_j(\omega)E_k(\omega) +$$
$$\sum_{j,k} \chi_{ijk}^{eem}(2\omega, \omega, \omega)E_j(\omega)B_k(\omega) \quad (6)$$

$$M_i(2\omega) = \sum_{j,k} \chi_{ijk}^{mee}(2\omega, \omega, \omega)E_j(\omega)E_k(\omega) \quad (7)$$

where i, j, and k represent the Cartesian coordinates for the laboratory frame, ω is the carrier frequency of the fundamental wave, E is the electric field, and B is the magnetic induction of the incident light. χ represents the nonlinear susceptibility tensor where the first superscript refers to the harmonic wave and the second two terms represent the fundamental waves. The indices in the superscript, e and m, represent electric- and magnetic-dipolar transitions, respectively. It is important to note that eqs 6 and 7 represent general formalisms for describing second harmonic generation by a system with both electric and magnetic dipolar contributions. For plasmon-mediated SHG, inclusion of local field gradients and multipolar terms may be necessary to fully describe the nonlinear optical response. The purpose here is to demonstrate the effectiveness of the PRG for examining the phase-dependent nonlinear optical responses of single nanostructures. In this context, the intensity of the SH field can be expressed by including P and M as nonlinear sources as follows:[37]

$$I(2\omega) = |FE_P^2(\omega) + GE_S^2(\omega) + HE_p(\omega)E_s(\omega)|^2 \quad (8)$$

where F, G, and H represent linear combinations of the nonlinear susceptibility tensors χ^{eee}, χ^{eem}, and χ^{mee} and are generally complex valued. $E_p(\omega)$ and $E_s(\omega)$ denote the P- and S-polarization components of the electric field vector of the fundamental wave. The P-laboratory frame was defined to be parallel to the bowtie interparticle axis. This axis is determined experimentally by changing the orientation of linearly polarized fundamental light using a half-wave plate in the absence of a quarter-wave plate. Equation 8 can be modified to include the experimentally controllable parameter, φ, by expressing $E_p(\omega)$ and $E_s(\omega)$ in terms of φ:

$$E_P(\omega) = E_0(\cos^2 \varphi + i \sin^2 \varphi) = P(\varphi) \quad (9)$$

$$E_S(\omega) = E_0(1 - i)\sin \varphi \cos \varphi = S(\varphi) \quad (10)$$

These substitutions transform eq 8 into:

$$I(2\omega) = I(\varphi) = |FP^2(\varphi) + GS^2(\varphi) + HP(\varphi)S(\varphi)|^2 \quad (11)$$

Using eq 11, the single-particle coefficients F, G, and H were quantified by analyzing the experimentally measured SHG intensity with respect to φ, which is changed with high precision by temporally delaying the orthogonal pulse pair as illustrated in Figure 9. Taking the ratio of the magnitudes of the magnetic-dipolar to electric-dipolar coefficients (G/F) provided a metric for determining the relative contribution of magnetic- to electric-dipolar character in the nonlinear signal. A higher G/F value translates to more dominant magnetic-dipolar contributions in the NLO signal.

SHG-CPV data collected for both asymmetric and symmetric gold bowtie structures are depicted in Figure 13.[41] These data represent two general cases that were observed experimentally. The SHG-CPV line shapes were fit to eq 11 to determine the F, G, and H coefficient magnitudes, and the fitting results are
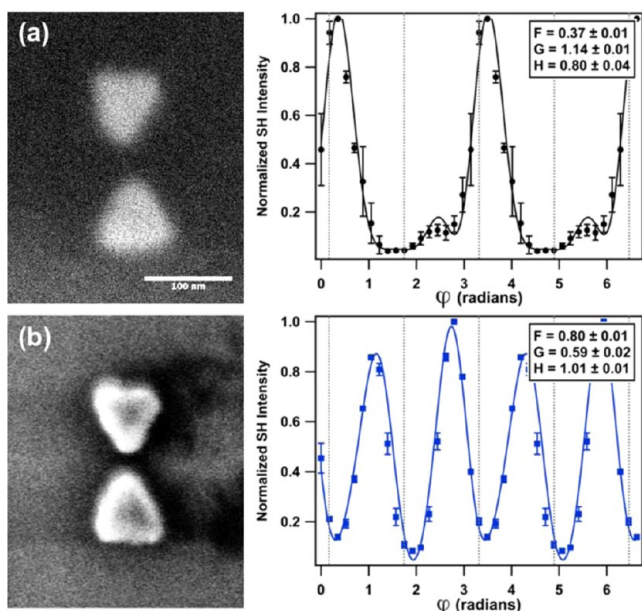
Figure 13. Comparison of second harmonic generation-detected continuous polarization variation data for (a) asymmetric and (b) symmetric gold bowtie nanostructures. SEM images for both bowtie structures are given in the left panel for both (a and b). Representative normalized intensities for the SHG signal is plotted versus the excitation phase shift of the fundamental in the left panel for both structures. The asymmetric bowtie (a) showed a less symmetric second harmonic phase-dependent line shape, reflecting larger relative magnetic dipolar contributions to the nonlinear optical response for (a) than for (b). The values of F, G, and H were quantified using eq 11 and are reported in the left panel inset for both samples. Adapted from ref 41. Copyright 2014 American Chemical Society.

presented in the legend of each panel. The vertical dashed lines in the plots represent phase shifts resulting in LCP and RCP light. Figure 13a (right side) shows a highly asymmetric line shape. In this case, the SHG intensity observed following LCP excitation was much greater than that observed following RCP excitation. The G/F ratio was 3.0 ± 0.1, indicating that magnetic dipoles contributed more to the NLO signal than did electric dipoles. The response of this asymmetrical nanostructure was highly sensitive to the incident polarization state, with the largest signal noted when one circularly polarized state of light was used. A 95% decrease in intensity was observed when the fundamental was changed from LCP to RCP, and a 75% decrease in intensity was seen following the shift from LCP to linearly polarized light.[41] The nanostructure used for the data in Figure 13b yielded a more symmetric line shape. The G/F ratio of this data was 0.73 ± 0.03.[41] Although a nonzero value of G was obtained, meaning that there was a magnetic-dipolar component to the NLO signal, this value for G/F suggested that the electric-dipolar component dominated the NLO signal for the symmetrical system. The NLO response from this bowtie was not selective to one circularly polarized state of light over the other; it had the greatest intensity when excited with linearly polarized light.

The specificity of the SHG-CPV data exemplifies the utility of advanced nonlinear optical methods for examining structural influences on plasmonic-electromagnetic interactions. The symmetric nanostructure can be approximated as two equilateral triangles (base = 75 nm and rise = 85 nm) arranged in a bowtie geometry and separated by 20 nm. The symmetric

structure has 2-fold axis of rotation, inversion, and symmetric reflection symmetry elements. The asymmetric structure was formed by lateral displacement of one triangle by 10 nm, which reduced the symmetry of the nanostructure. As a result, the asymmetric bowtie interacts selectively with left circularly polarized light due to increased magnetic dipolar contributions to the nonlinear optical response, as revealed by the SHG-CPV analysis. These data demonstrate the insight single-particle NLO imaging can provide for understanding how nanoscale structure can be used for selective interaction with and amplification of specific polarization states of electromagnetic energy.

3c. Electronic Energy Relaxation of Electromagnetically Coupled Plasmonic Nanoparticles. Structure-specific descriptions for electronic energy relaxation are essential to determining how nanoparticle assemblies use electromagnetic energy. The current state-of-the-art for these quantifications come from single-particle dark-field microscopy measurements, from which the line width (Γ) of a Lorentzian scattering peak can be converted to the electronic dephasing time (T_2).[110,111] This method is very effective for examining electronic relaxation in isolated nanoparticles[111] and has recently been extended to accurately determine rates for interfacial electron transfer between gold nanorods and graphene.[124] For networks of electromagnetically coupled plasmonic nanoparticles, the scattering spectrum can become very complicated, making line width deconvolution difficult. Therefore, a direct experimental measurement capable of resolving electronic relaxation rates for these systems is desired.

In this section, the use of collinear, parallel phase-locked pulse replicas for femtosecond time-resolved microscopy of single nanostructures is described. The optical response function of a system, $R(t)$, describes the interaction between a stimulating optical field $E(t)$ and the material. The induced optical polarization is described as a convolution of the response function and the optical field, given by $P(t) = \int R(t - t')E(t') \, dt'$. The amplitude and phase of the system response can be determined using interferometric frequency-resolved optical gating (IFROG) to measure $I_{\text{IFROG}}(2\omega, \tau) \propto |\int [X(t) + X(t - \tau)]^2 \exp(-i\omega t) \, dt|^2$ with time delay τ and frequency ω.[109] For a nonlinear medium that is far from resonance, the measured response is essentially instantaneous, and the output signal is proportional to the electric field of the input laser pulse, $E(t)$, gated by the time-delayed pulse $E(t - \tau)$. In order to perform these measurements, we first corrected for dispersion introduced by the optics used for pulse replication and imaging. The laser pulse width is compressed to sub-20 fs. If the material has a resonance at the frequency of the excitation source, as is the case for plasmon-resonant excitation, the finite response time leads to an induced polarization transient, and the output signal is a convolution of the driving laser pulse, $E(t)$, and the resonance response function, $R(t)$, given by $P(t) = E(t) \otimes R(t) = \int R(t - t')E(t') \, dt'$. To determine $R(t)$, the resonance response function of a system, we measured $E(t)$ from a nonresonant sample and $P(t)$ from a plasmonic nanostructure and performed a standard deconvolution. The plasmonic response is modeled as a damped harmonic oscillator in the time domain, $R(t) = A \exp(i\omega_{\text{LSPR}}t - \gamma t)$, where A gives the effective oscillator strength, ω_{LSPR} is the plasmon resonance frequency, and γ is the line width described by $\gamma = 1/T_2$, where T_2 is the plasmon dephasing time.

Multidimensional IFROG traces (Figure 14a) were measured by collecting second harmonic spectra as a function of
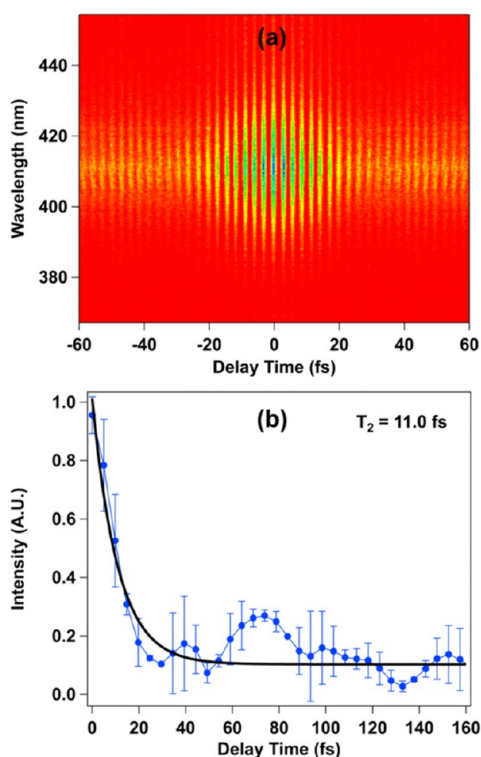
Figure 14. Summary of spectral interferometric analysis of plasmon-resonant SHG signals. (a) Plot of the second harmonic generation wavelength plotted versus the excitation interpulse delay time. (b) Plasmon dephasing data (filled blue ●) and fit (black line) extracted from (a) as described in the text.

Table 1. Summary of Results from Three Different Nanoparticle Dimers[a]

	LSPR (eV)	Γ (meV)	dark-field T_2 (fs)	IFROG T_2 (fs)
particle 1	1.57	157	8.3	12.5
particle 2[b]	1.54	109	11.9	11.0
particle 3	1.61	154	8.5	10.5

[a]The LSPR energy, homogeneous line width, and plasmon dephasing time from both dark-field line width analysis and IFROG analysis are presented. [b]The dark-field spectrum from this particle is presented in Figure 15a as the red trace. The IFROG data and resonance response in Figure 14 and the SEM image in Figure 15b are also from this nanostructure.

interpulse time delay induced by the PRG. The signal was acquired for a ±300 fs time window using 0.30 fs delay steps. The total acquisition time for one IFROG spectrogram in Figure 13a was approximately 2 min. The IFROG traces were processed by extracting the DC components via Fourier filtering. Upon extraction, the DC portion was treated as a standard FROG trace; it was first binned into a 128 × 128-point spectrogram and then processed via a home-written singular value decomposition (SVD)-based FROG reconstruction algorithm to determine the amplitude and phase of the response, $X(t)$.[125]

The data shown in Figure 14a were obtained via plasmon-resonant SHG from gold nanoparticle homodimers; 60 nm diameter solid gold nanospheres were dimerized using benzene-dithiol, as previously described.[51] The homodimer is chosen as a model nanoparticle assembly because the interparticle resonance gives a simple scattering spectrum, so that scattering line width and nonlinear time-domain measurements could be compared. Using time- and energy-resolved SHG data for these particles, we first measured $P(t)$. To extract $R(t)$, we measured the nonresonant response from the microscope coverslip to obtain $E(t)$. Deconvolution was performed by transforming $P(t)$ and $E(t)$ from the time domain to the frequency domain. $P(\omega) = E(\omega)R(\omega)$, and $R(\omega)$ was calculated by division. Upon inverse Fourier transformation of $R(\omega)$ to yield $R(t)$, the dephasing time was determined directly by fitting $R(t)$ to an exponential function. The dephasing times retrieved from three different resonantly excited homodimers were 10.5, 11.0, and 12.5 fs, as reported in Table 1. One example of the retrieved resonance response decay is given in Figure 14b.

In order to assess the accuracy of our single nanoparticle dimer IFROG analysis, we correlated these results to T_2 values obtained from dark-field line width analysis of the same samples. Figure 15 shows dark-field scattering spectra from three different nanoparticle dimers with LSPRs spanning 1.5 to 2.0 eV. A representative solid gold nanosphere SEM image, corresponding to the structure that produced the red data in Figure 15a, is given in Figure 15b. Dark-field microscopy was used to screen particles and find those with a LSPR "on" and "off" resonance with the fundamental carrier wave of the laser (1.54 eV). The dark-field spectra were fit to a Lorentzian function $I(\omega) = C_0/[(\omega - \omega_0)^2 + \Gamma^2/4]$ to determine both the localized surface plasmon resonance frequency, ω_0, and the homogeneous line width, Γ. The plasmon dephasing time, T_2, was calculated from the homogeneous line width as $T_2 = 2\hbar/\Gamma$. The results from dark-field scattering line width analysis and single-particle SHG-detected IFROG agreed well and are summarized in Table 1. These data demonstrate that combining the PRG with a nonlinear optical microscope yields a powerful tool capable of determining dynamics information from single nanoparticle assemblies. This time-domain approach has tremendous potential for examining nanoparticle assemblies with complex scattering spectra, for which it is difficult to analyze dephasing rates using only frequency-resolved data.

In addition to second harmonic generation from nanoparticle assemblies, we have also used nanoparticle two-photon photoluminescence (TPPL) to monitor electron dynamics. In order to isolate the TPPL signal from SHG signals, we used a 475 nm long-pass filter (chroma). The TPPL spectrum from a single nanoparticle assembly excited at several excitation pulse powers is shown in Figure 3c. A broad emission spectrum spanning the visible region of the electromagnetic spectrum with a maximum at approximately 675 nm was observed. The peak is abruptly cut off at 680 nm due to an excitation filter that extinguishes the fundamental photons. Figure 3d shows the log of the TPPL signal intensity vs the log of the incident laser power. The value of the slope was 2.06 ± 0.02, confirming the quadratic power dependence expected for TPPL. As seen at the top of Figure 3c, the TPPL signal was second order with respect to incident laser power across the entire TPPL spectrum. The same power-dependence analysis was carried out using the image contrast of the point-spread function, and a second-order power dependence was obtained once more. These measurements confirmed that we observed a two-photon excitation process, which we attributed to two-photon photoluminescence.

More insight into the TPPL mechanism was obtained from polarization-dependent and time-resolved interferometric non-
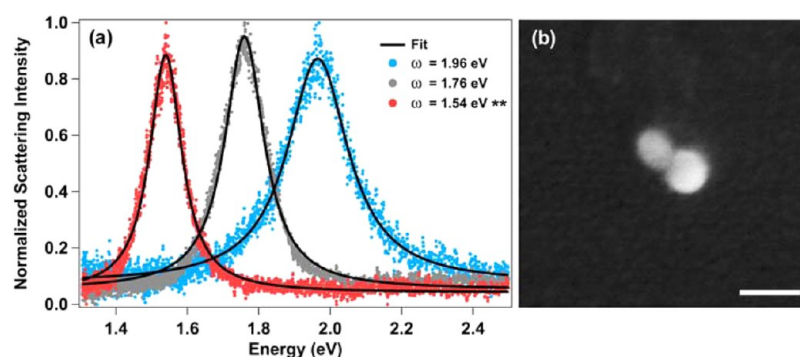
Figure 15. (a) Scattering spectra obtained for three different nanoparticle dimers using single-particle dark-field microscopy. The black lines correspond to Lorentzian fits to the scattering spectra, which were used to determine the center scattering energy (ω) and line width (Γ). (b) Representative SEM image of a solid gold nanosphere dimer. This particular image corresponds to the structure that yielded the red scattering data (ω = 1.54 eV) in (a). The scale bar represents 100 nm.
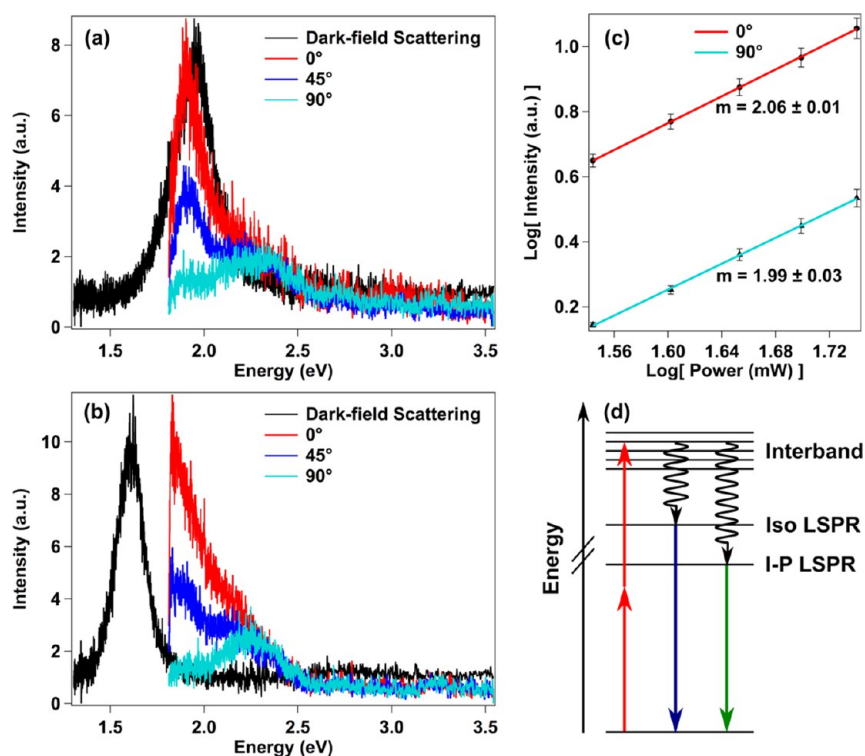

Figure 16. (a and b) Plot of energy-resolved dark-field (black) and TPPL emission obtained from two different dimers of 60 nm diameter solid gold nanospheres following excitation by two 800 nm photons. The TPPL spectra were acquired by filtering emission using a linear polarizer aligned at 0° (red), 45° (blue), and 90° (cyan) with respect to the dimer interparticle axis; excitation pulses were aligned parallel to the dimer interparticle axis for all measurements. The polarization-dependent emission signal revealed two peaks for both samples. (c) Plot of the log of the integrated intensity of the TPPL signal for both the high-energy (cyan) and low-energy (red) peaks versus the log of incident laser power. The high- and low-energy peaks were isolated using polarization-selective detection. Both peaks yielded quadratic power dependencies. (d) Energy-level diagram depicting the TPPL mechanism. Two 800 nm photons excited the metal interband transition, which resulted in rapid carrier relaxation prior to radiative plasmon decay, as described in text.

linear optical imaging. Figure 16 (panels a and b) compare the energy-resolved dark-field scattering and TPPL spectra obtained from two different solid gold nanosphere dimers; both dimer samples were excited using two 800 nm photons. The red TPPL traces were collected by filtering the emission using a linear polarizer aligned along the dimer interparticle axis. For these spectra, close correspondences between the dark-field scattering and TPPL emission spectra were observed; the interparticle plasmon mode resonance determined from dark-field scattering matched the emission energy. In addition, a high-energy emission peak was detected for both dimers at

approximately 2.3 eV, which agreed well with the LSPR resonance of the individual nanospheres comprising the dimer. The blue and cyan spectra shown in Figure 16 (panels a and b) were obtained by rotating the linear polarizer that filtered the TPPL signal by 45 and 90 deg with respect to the dimer interparticle axis, respectively. The TPPL intensity of the low-energy peak was very sensitive to the polarizer angle and yielded a dipolar response similar to that obtained from dark-field scattering.[113] Therefore, the low-energy TPPL signal exhibited polarized emission. In contrast, the high-energy peak did not depend upon the polarizer angle but, rather, exhibited

isotropic emission, as is expected for the LSPR of an isolated metal nanosphere. These data indicated that the TPPL signals originated from plasmon-mode-specific radiative decay.[126−128]

In order to develop a mechanistic description of the origin of the TPPL signal, the excitation-power dependencies of both emission peaks were quantified using polarization-selective detection. The log of the integrated TPPL signal for both peaks is plotted versus the log of the 800 nm excitation power (Figure 16c). In both cases, quadratic power dependencies were obtained. The Figure 16c data were acquired using an interpulse time delay of zero. By using the PRG to temporally separate the laser pulses, the TPPL intensity power dependence for both pulses could be examined. From this study, we determined that two photons from the leading pulse excited the sample; the second pulse functioned as a local oscillator to amplify the nonlinear signal. Therefore, two 800 nm photons excited the interband transition of the SGN dimer. Following rapid relaxation, the carriers radiatively decayed by plasmon emission as described in Figure 16d.

The time-dependence of the TPPL signal was obtained interferometrically using emission-generated image contrast. Several nanoparticle dimers were surveyed for this study, which allowed us to examine the effects of matching the LSPR and laser frequencies. In order to examine the time-dependent TPPL signal resulting from plasmonic nanoparticles, the nonresonant interferometric SHG signal from the microscope slide was used as a reference. The interferometric traces for nonresonant reference SHG (black), and TPPL from resonant (red) and nonresonant (blue) dimers all remain in phase for the first few cycles of the laser pulse (Figure 17a, left). However, as the interpulse temporal delay was increased beyond several cycles of the excitation carrier wave, a phase shift was observed in the TPPL signal of resonant samples (Figure 17a, right). Thus, pulse characterization, phase correction, and reference comparison are critical when performing these measurements. Excitation pulses with uncorrected high-order dispersion will exhibit a phase shift at interpulse time delays exceeding a few optical cycles. The TPPL data presented here are referenced to the nonresonant SHG signal to ensure that laser pulse dispersion is not responsible for the observed phase shift. Therefore, the TPPL phase shift we detected for a single resonant nanoparticle dimer reflects electronic relaxation dynamics.

In Figure 17b, time-dependent TPPL-detected phase shifts resulting from nine different nanoparticle dimers are summarized. Dimers with LSPR that did not match the laser wavelength are designated with blue ●. Data from resonant dimers are depicted by red ■. Results from the two samples highlighted in Figure 17a are designated in Figure 17b using dashed lines and filled markers. Figure 17b data were obtained by subtracting the peak and trough arrival times of the reference SHG interferogram from the corresponding values for the TPPL fringes obtained from single nanoparticle samples. The time-dependent dynamics are reported as a time shift, Δt, as well as a relative phase shift. Collectively, we observed a phase difference between the TPPL and reference SHG fringes as the delay time was increased. The data show that the magnitude and time dependence of the phase shift was unique for each nanoparticle dimer. One generality that could be extracted from the data is that resonant nanoparticles showed the largest structure specificity for the time-dependent response; the behaviors of nonresonant samples were all similar. The largest relative phase shift we observed for
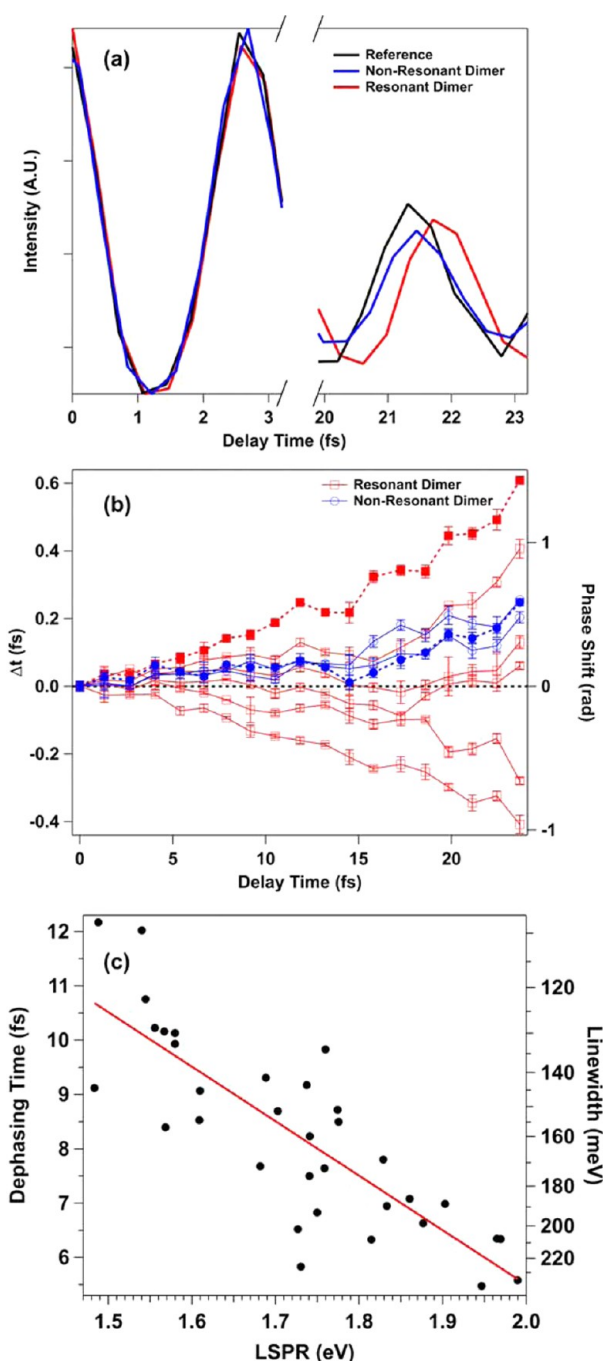

Figure 17. (a) Interferometric analysis of time-dependent two-photon photoluminescence signals. The TPPL signal was acquired from 2.6 to 1.8 eV emission energies for all samples. At early times, the photoluminescence signals from resonant (red) and nonresonant (blue) samples are in phase with the nonresonant second harmonic generation detected reference (black). For interpulse time delays exceeding 20 fs, the photoluminescence signal of resonant nanoparticles (red) exhibits a phase shift with respect to the reference signal (black). (b) Summary of the time dependence of the photoluminescence-detected phase shifts for nine different nanoparticle dimers. (c) Plasmon dephasing time (left) and line width (right) plotted versus interparticle LSPR resonance. The panel (c) data was obtained from single structure measurements of several dimers of 60 nm diamter solid gold nanospheres assembled using benzene-dithiol as an aggregating agent. The direct correspondence between plasmon dephasing time and scattering energy was reflected by a Pearson's coefficient of approximately 0.82 ± 0.10.

plasmon-resonant structures was approximately 1.4 radians, which was 250% greater than that observed for nonresonant systems.

Similar phase shifts are observed in interferometrically detected molecular stimulated-fluorescence emission.[129] These shifts are attributed to time-dependent electronic relaxation dynamics. The structure-dependent phase shifts observed for SGN dimers reflected differences in carrier dynamics. One possible explanation for the distinct behavior of resonant and nonresonant dimers arises from plasmon dephasing by scattering with interband states. By comparison, the non-resonant samples examined in this study have interparticle plasmonic frequencies that are closer in energy to the interband transition than those of the resonant samples. As a result, the plasmon mode would dephase very rapidly for the nonresonant sample. Experimental evidence in support of this hypothesis is given in Figure 17c, which compares the LSPR line width (and dephasing time) to the LSPR energy; samples with plasmon resonances energetically closer to the interband transition exhibit more rapid dephasing times than those structures for which the energy difference between interband and intraband LSPR excitations is large. Because the nonresonant samples dephase rapidly due to interband scattering, no significant phase shift is detectable within 20 fs after two-photon excitation. A second possible cause for the difference in the time-dependent TPPL responses observed for resonant and nonresonant samples is plasmon-mediated emission. As noted above, the second laser pulse in the sequence serves as a local oscillator. If the plasmon modulates the TPPL emission, the sensitivity of the second laser pulse to these dynamics may depend upon resonance matching of the laser carrier wave and the nanoparticle mode. Future time-resolved nonlinear interferometric single-structure imaging experiments are critical for understanding these different structure-dependent relaxation mechanisms.

Single-particle TPPL-based interferometric imaging has great potential for understanding plasmon dynamics for systems under strong interparticle electromagnetic coupling. For structures that exhibit complex hybridized mode structures, interferometric data has the capacity to reveal mode-specific beating patterns, which should be revealed through time-dependent phase shifts in the emission signal. In this way, the influence of plasmon-mode composition on electron dynamics can be examined. From a technical point of view, the photoluminescence-based interferometric detection using phase-locked ultrashort laser pulses extends the timescales of time-resolved fluorescence imaging to time domains that are difficult to access using alternative methods.

4. SUMMARY AND OUTLOOK

Several recent advances that can be used for understanding nanostructure-specific interactions between nanoparticles and electromagnetic energy have been described in this article. These advances have been made possible by breakthroughs in nonlinear optical microscopy using ultrabroadband laser pulses that expand the plasmonic nanoparticle imaging platform. Nonlinear optical methods that allow nanoparticle imaging with nanometer spatial accuracies and the information content achievable using sequences of phase-stabilized laser pulses are likely to play an important role in describing the use and control of electromagnetic energy at the nanoscale. For example, the localization measurements that enable pinpointing the polarization-dependent position of harmonic hot spots in

trimeric plasmon nanolens structures can be applied to imaging more sophisticated nanoparticle networks. By acquiring these images with temporally delayed pulses, new insights into plasmon-mode-specific energy localization can be obtained. Because the plasmon dephasing rates are determined by both the relative amplitudes and the decay rates of interfering resonances, time-resolved TPPL- and SHG-detected spectral interferometric images obtained from individual nanoparticle assemblies can be used to determine how interparticle resonances transport and confine energy on the nanoscale. Important questions in plasmon dynamics involve under-standing how the electronic relaxation of coupled particles differs from that of isolated nanoparticles. For molecular systems, interchromophore energy-transfer dynamics are determined by the coupling strengths between neighboring molecules. Molecules that are strongly coupled exhibit coherent energy transport, whereas weakly coupled systems thermalize internally prior to classical energy transfer from an equilibrium phonon bath.[130] The nanoparticle imaging methods that combine high temporal resolution and spatial accuracy described in this article can be used to examine how specific interparticle plasmon modes mediate nanoscale electromagnetic energy transfer and how they compete with internal thermalization of the individual nanoparticle building blocks.

Plasmon amplification of chiro-optical signals is an especially promising area for future research. Several examples of plasmon-enhanced circular dichroism and optical activity exist.[38,39,41,88,120−122,131−136] However, it has only been possible to acquire optical images using circular dichroism-based contrast with nanometer spatial accuracy in a few instances.[41,88] The difficulties of CD imaging stem from the challenges of preserving the circularly polarized state of light when working with conventional far-field microscopes. The generation of a circularly polarized excitation source by using an orthogonal pair of phase-locked temporally delayed laser pulses as described in Section 3b solves many of the challenges of CD imaging. This mode of imaging is general and can be easily adapted to examine other nonlinear optical processes. For example, third-order coherent Raman signals can be detected using essentially the same experimental setup as we have used for second-order CD imaging. Coherent Raman signals can be significantly amplified using plasmonic Fano resonances, allowing single-molecule detection.[76] In fact, these stimulated nonlinear signals are shown to be more responsive to plasmon amplification than spontaneous Raman scattering.[76] Because the localization accuracy of optical signals increases with the number of photons detected,[117] circular dichroism images generated from coherent Raman signals produced by phase-locked broad-bandwidth laser pulses have the capacity to provide vibrational-mode and molecular-structure-specific imaging with maximal spatial accuracy. These vibrational circular dichroism signals can be amplified further by applied magnetic fields.[137] Therefore, the spatial accuracy of these CD images could be enhanced by incorporation of magnetic fields in the nonlinear imaging platform. Strategies for extracting magnetic resonance and electron spin information from coherent Raman signals detected using applied magnetic fields are known.[138−141] Therefore, merging the magneto- and nonlinear-optical platforms has the potential to provide magnetic resonance and electron spin-based imaging with the spatial resolution and accuracy achievable by optical methods, far surpassing the typical spatial limitations of conventional magnetic resonance imaging.

AUTHOR INFORMATION

Corresponding Author

*E-mail: klk@chem.fsu.edu.

Author Contributions

The manuscript was written through contributions of all authors. All authors have given approval to the final version of the manuscript.
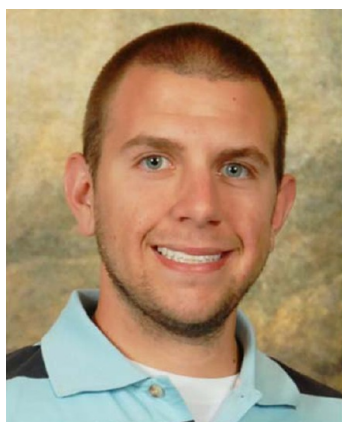
Notes

The authors declare no competing financial interest.

Biographies

Jeremy W. Jarrett is a Ph.D. candidate in Chemistry at Florida State University working under the supervision of Kenneth L. Knappenberger, Jr. He received his B.S. in Chemistry from Florida State University in 2011. His primary research interests include nonlinear optics and single particle spectroscopy.

Tian Zhao received his B. Eng. in Applied Chemistry from Hebei Normal University, China, in 2009 and M. Sc. in Applied Chemistry from Beihang University, China, in 2012. He is currently enrolled in the Ph.D. program in the Department of Chemistry and Biochemistry at Florida State University where he studies nanophotonic systems using single-particle nonlinear optical microscopy under the supervision of Kenneth L. Knappenberger, Jr.

Jeffrey S. Johnson received his B. Sc. in Chemical Physics from St. Cloud State University in 2014. He joined the Knappenberger group as a graduate student at Florida State University in 2014. His research interests include nanoparticle plasmonics, single particle spectroscopy, and magneto-optics.

Kenneth L. Knappenberger, Jr. is an Associate Professor at Florida State University. He received his B.S. in Chemistry from Lock Haven University in 2000 and his Ph.D. in Chemistry from the Pennsylvania State University in 2005, upon completing his dissertation work on ultrafast electron dynamics in cluster systems with A.W. Castleman, Jr. He was a postdoctoral researcher with Steve Leone at University of California, Berkeley, from 2005 to 2008. His research group at Florida State University (http://www.chem.fsu.edu/~klk/KLK_group/) focuses on understanding the structural influences on the optical and electronic properties of photonic nanomaterials, through nonlinear and magneto-optical spectroscopy studies.

ACKNOWLEDGMENTS

■ REFERENCES

(1) Stockman, M. I.; Faleev, S. V.; Bergman, D. J. Coherently Controlled Femtosecond Energy Localization on Nanoscale. *Appl. Phys. B: Lasers Opt.* **2002**, *74*, S63–S67.

(2) Stockman, M. I.; Faleev, S. V.; Bergman, D. J. Coherent Control of Femtosecond Energy Localization in Nanosystems. *Phys. Rev. Lett.* **2002**, *88*, 4.

(3) Li, K. R.; Stockman, M. I.; Bergman, D. J. Self-Similar Chain of Metal Nanospheres as an Efficient Nanolens. *Phys. Rev. Lett.* **2003**, *91*, 4.

(4) Stockman, M. I.; Faleev, S. V.; Bergman, D. J. Femtosecond Energy Concentration in Nanosystems: Coherent Control. *Phys. B (Amsterdam, Neth.)* **2003**, *338*, 361–365.

(5) Stockman, M. I.; Bergman, D. J.; Kobayashi, T. Coherent Control of Nanoscale Localization of Ultrafast Optical Excitation in Nanosystems. *Phys. Rev. B* **2004**, *69*, 10.

(6) Li, K. R.; Stockman, M. I.; Bergman, D. J. Enhanced Second Harmonic Generation in a Self-Similar Chain of Metal Nanospheres. *Phys. Rev. B* **2005**, *72*, 4.

(7) Mirkin, C. A.; Letsinger, R. L.; Mucic, R. C.; Storhoff, J. J. A DNA-Based Method for Rationally Assembling Nanoparticles into Macroscopic Materials. *Nature* **1996**, *382*, 607–609.

(8) Jensen, T. R.; Schatz, G. C.; Van Duyne, R. P. Nanosphere Lithography: Surface Plasmon Resonance Spectrum of a Periodic Array of Silver Nanoparticles by Ultraviolet-Visible Extinction Spectroscopy and Electrodynamic Modeling. *J. Phys. Chem. B* **1999**, *103*, 2394–2401.

(9) Piner, R. D.; Zhu, J.; Xu, F.; Hong, S. H.; Mirkin, C. A. "Dip-Pen" Nanolithography. *Science* **1999**, *283*, 661–663.

(10) Jensen, T. R.; Malinsky, M. D.; Haynes, C. L.; Van Duyne, R. P. Nanosphere Lithography: Tunable Localized Surface Plasmon Resonance Spectra of Silver Nanoparticles. *J. Phys. Chem. B* **2000**, *104*, 10549–10556.

(11) Haynes, C. L.; Van Duyne, R. P. Nanosphere Lithography: A Versatile Nanofabrication Tool for Studies of Size-Dependent Nanoparticle Optics. *J. Phys. Chem. B* **2001**, *105*, 5599–5611.

(12) Wang, Q.; Nealey, P. F.; de Pablo, J. J. Behavior of Single Nanoparticle/Homopolymer Chain in Ordered Structures of Diblock Copolymers. *J. Chem. Phys.* **2003**, *118*, 11278–11285.

(13) Radloff, C.; Halas, N. J. Plasmonic Properties of Concentric Nanoshells. *Nano Lett.* **2004**, *4*, 1323–1327.

(14) Zhang, H.; Mirkin, C. A. Dpn-Generated Nanostructures Made of Gold, Silver, and Palladium. *Chem. Mater.* **2004**, *16*, 1480–1484.

(15) Rosi, N. L.; Mirkin, C. A. Nanostructures in Biodiagnostics. *Chem. Rev. (Washington, DC, U.S.)* **2005**, *105*, 1547–1562.

(16) Liz-Marzan, L. M. Tailoring Surface Plasmons Through the Morphology and Assembly of Metal Nanoparticles. *Langmuir* **2006**, *22*, 32–41.

(17) Wang, H.; Halas, N. J. Plasmonic Nanoparticle Heterodimers in a Semiembedded Geometry Fabricated by Stepwise Upright Assembly. *Nano Lett.* **2006**, *6*, 2945–2948.

(18) Henzie, J.; Lee, M. H.; Odom, T. W. Multiscale Patterning of Plasmonic Metamaterials. *Nat. Nanotechnol.* **2007**, *2*, 549–554.

(19) Tao, A. R.; Ceperley, D. P.; Sinsermsuksakul, P.; Neureuther, A. R.; Yang, P. D. Self-Organized Silver Nanoparticles for Three-Dimensional Plasmonic Crystals. *Nano Lett.* **2008**, *8*, 4033–4038.

(20) Henzie, J.; Lee, J.; Lee, M. H.; Hasan, W.; Odom, T. W. Nanofabrication of Plasmonic Structures. *Annu. Rev. Phys. Chem.* **2009**, *60*, 147–165.

(21) Son, J. G.; Bae, W. K.; Kang, H.; Nealey, P. F.; Char, K. Placement Control of Nanomaterial Arrays on the Surface-Reconstructed Block Copolymer Thin Films. *ACS Nano* **2009**, *3*, 3927–3934.

(22) Fan, J. A.; Wu, C.; Bao, K.; Bao, J.; Bardhan, R.; Halas, N. J.; Manoharan, V. N.; Nordlander, P.; Shvets, G.; Capasso, F. Self-Assembled Plasmonic Nanoparticle Clusters. *Science* **2010**, *328*, 1135–1138.

(23) Barrow, S. J.; Funston, A. M.; Gomez, D. E.; Davis, T. J.; Mulvaney, P. Surface Plasmon Resonances in Strongly Coupled Gold Nanosphere Chains from Monomer to Hexamer. *Nano Lett.* **2011**, *11*, 4180–4187.

(24) Lee, M. H.; Huntington, M. D.; Zhou, W.; Yang, J. C.; Odom, T. W. Programmable Soft Lithography: Solvent-Assisted Nanoscale Embossing. *Nano Lett.* **2011**, *11*, 311–315.

(25) Nepal, D.; Onses, M. S.; Park, K.; Jespersen, M.; Thode, C. J.; Nealey, P. F.; Vaia, R. A. Control Over Position, Orientation, and Spacing of Arrays of Gold Nanorods Using Chemically Nanopatterned Surfaces and Tailored Particle-Particle-Surface Interactions. *ACS Nano* **2012**, *6*, 5693–5701.

(26) Zhang, C.; Zhou, Y.; Merg, A.; Song, C.; Schatz, G. C.; Rosi, N. L. Hollow Spherical Gold Nanoparticle Superstructures with Tunable Diameters and Visible to Near-Infrared Extinction. *Nanoscale* **2014**, *6*, 12328–12332.

(27) Murphy, C. J.; San, T. K.; Gole, A. M.; Orendorff, C. J.; Gao, J. X.; Gou, L.; Hunyadi, S. E.; Li, T. Anisotropic Metal Nanoparticles: Synthesis, Assembly, and Optical Applications. *J. Phys. Chem. B* **2005**, *109*, 13857–13870.

(28) Prodan, E.; Radloff, C.; Halas, N. J.; Nordlander, P. A Hybridization Model for the Plasmon Response of Complex Nanostructures. *Science* **2003**, *302*, 419–422.

(29) Nordlander, P.; Oubre, C.; Prodan, E.; Li, K.; Stockman, M. I. Plasmon Hybridizaton in Nanoparticle Dimers. *Nano Lett.* **2004**, *4*, 899–903.

(30) Prodan, E.; Nordlander, P. Plasmon Hybridization in Spherical Nanoparticles. *J. Chem. Phys.* **2004**, *120*, 5444–5454.

(31) Brandl, D. W.; Oubre, C.; Nordlander, P. Plasmon Hybridization in Nanoshell Dimers. *J. Chem. Phys.* **2005**, *123*, 24701.

(32) Brandl, D. W.; Mirin, N. A.; Nordlander, P. Plasmon Modes of Nanosphere Trimers and Quadrumers. *J. Phys. Chem. B* **2006**, *110*, 12302–12310.

(33) Willingham, B.; Brandl, D. W.; Nordlander, P. Plasmon Hybridization in Nanorod Dimers. *Appl. Phys. B: Lasers Opt.* **2008**, *93*, 209–216.

(34) Jain, P. K.; El-Sayed, M. A. Plasmonic Coupling in Noble Metal Nanostructures. *Chem. Phys. Lett.* **2010**, *487*, 153–164.

(35) Sheikholeslami, S.; Jun, Y. W.; Jain, P. K.; Alivisatos, A. P. Coupling of Optical Resonances in a Compositionally Asymmetric Plasmonic Nanoparticle Dimer. *Nano Lett.* **2010**, *10*, 2655–2660.

(36) Halas, N. J.; Lal, S.; Chang, W. S.; Link, S.; Nordlander, P. Plasmons in Strongly Coupled Metallic Nanostructures. *Chem. Rev. (Washington, DC, U.S.)* **2011**, *111*, 3913–3961.

(37) Kauranen, M.; Verbiest, T.; Persoons, A. Second-Order Nonlinear Optical Signatures of Surface Chirality. *J. Mod. Opt.* **1998**, *45*, 403–423.

(38) Chandra, M.; Dowgiallo, A. M.; Knappenberger, K. L., Jr. Magnetic Dipolar Interactions in Solid Gold Nanosphere Dimers. *J. Am. Chem. Soc.* **2012**, *134*, 4477–4480.

(39) Chandra, M.; Knappenberger, K. L., Jr. Nanoparticle Surface Electromagnetic Fields Studied by Single-Particle Nonlinear Optical Spectroscopy. *Phys. Chem. Chem. Phys.* **2013**, *15*, 4177–4182.

(40) Valev, V. K.; Baumberg, J. J.; Sibilia, C.; Verbiest, T. Chirality and Chiroptical Effects in Plasmonic Nanostructures: Fundamentals, Recent Progress, and Outlook. *Adv. Mater. (Weinheim, Ger.)* **2013**, *25*, 2517–2534.

(41) Jarrett, J. W.; Herbert, P. J.; Dhuey, S.; Schwartzberg, A. M.; Knappenberger, K. L., Jr. Chiral Nanostructures Studied Using Polarization-Dependent Noles Imaging. *J. Phys. Chem. A* **2014**, *118*, 8393–8401.

(42) Hao, E.; Schatz, G. C. Electromagnetic Fields around Silver Nanoparticles and Dimers. *J. Chem. Phys.* **2004**, *120*, 357–366.

(43) Jain, P. K.; El-Sayed, M. A. Universal Scaling of Plasmon Coupling in Metal Nanostructures: Extension from Particle Pairs to Nanoshells. *Nano Lett.* **2007**, *7*, 2854–2858.

(44) Nome, R. A.; Guffey, M. J.; Scherer, N. F.; Gray, S. K. Plasmonic Interactions and Optical Forces Between Au Bipyramidal Nanoparticle Dimers. *J. Phys. Chem. A* **2009**, *113*, 4408–4415.

(45) Reinhard, B. M.; Siu, M.; Agarwal, H.; Alivisatos, A. P.; Liphardt, J. Calibration of Dynamic Molecular Rule Based on Plasmon Coupling Between Gold Nanoparticles. *Nano Lett.* **2005**, *5*, 2246−2252.

(46) Sonnichsen, C.; Reinhard, B. M.; Liphardt, J.; Alivisatos, A. P. A Molecular Ruler Based on Plasmon Coupling of Single Gold and Silver Nanoparticles. *Nat. Biotechnol.* **2005**, *23*, 741−745.

(47) Liu, N.; Hentschel, M.; Weiss, T.; Alivisatos, A. P.; Giessen, H. Three-Dimensional Plasmon Rulers. *Science* **2011**, *332*, 1407−1410.

(48) Bourret, G. R.; Ozel, T.; Blaber, M.; Shade, C. M.; Schatz, G. C.; Mirkin, C. A. Long-Range Plasmophore Rulers. *Nano Lett.* **2013**, *13*, 2270−2275.

(49) Knappenberger, K. L., Jr.; Schwartzberg, A. M.; Dowgiallo, A.-M.; Lowman, C. A. Electronic Relaxation Dynamics in Isolated and Aggregated Hollow Gold Nanospheres. *J. Am. Chem. Soc.* **2009**, *131*, 13892.

(50) Chandra, M.; Dowgiallo, A.-M.; Knappenberger, K. L., Jr. Two-Photon Rayleigh Scattering from Isolated and Aggregated Hollow Gold Nanospheres. *J. Phys. Chem. C* **2010**, *114*, 19971−19978.

(51) Chandra, M.; Dowgiallo, A.-M.; Knappenberger, K. L., Jr. Controlled Plasmon Resonance Properties of Hollow Gold Nanosphere Aggregates. *J. Am. Chem. Soc.* **2010**, *132*, 15782−15789.

(52) Stagg, S. M.; Knappenberger, K. L.; Dowgiallo, A.-M.; Chandra, M. Three-Dimensional Interfacial Structure Determination of Hollow Gold Nanosphere Aggregates. *J. Phys. Chem. Lett.* **2011**, *2*, 2946−2950.

(53) Lassiter, J. B.; Aizpurua, J.; Hernandez, L. I.; Brandl, D. W.; Romero, I.; Lal, S.; Hafner, J. H.; Nordlander, P.; Halas, N. J. Close Encounters between Two Nanoshells. *Nano Lett.* **2008**, *8*, 1212−1218.

(54) Perez-Gonzalez, O.; Zabala, N.; Borisov, A. G.; Halas, N. J.; Nordlander, P.; Aizpurua, J. Optical Spectroscopy of Conductive Junctions in Plasmonic Cavities. *Nano Lett.* **2010**, *10*, 3090−3095.

(55) Song, P.; Nordlander, P.; Gao, S. Quantum Mechanical Study of the Coupling of Plasmon Excitations to Atomic-Scale Electron Transport. *J. Chem. Phys.* **2011**, *134*, 074701.

(56) Luk'yanchuk, B.; Zheludev, N. I.; Maier, S. A.; Halas, N. J.; Nordlander, P.; Giessen, H.; Chong, C. T. The Fano Resonance in Plasmonic Nanostructures and Metamaterials. *Nat. Mater.* **2010**, *9*, 707−715.

(57) Lassiter, J. B.; Sobhani, H.; Knight, M. W.; Mielczarek, W. S.; Nordlander, P.; Halas, N. J. Designing and Deconstructing the Fano Lineshape in Plasmonic Nanoclusters. *Nano Lett.* **2012**, *12*, 1058−1062.

(58) Biswas, S.; Duan, J.; Nepal, D.; Park, K.; Pachter, R.; Vaia, R. A. Plasmon-Induced Transparency in the Visible Region Via Self-Assembled Gold Nanorod Heterodimers. *Nano Lett.* **2013**, *13*, 6287−6291.

(59) Biswas, S.; Duan, J. S.; Nepal, D.; Pachter, R.; Vaia, R. Plasmonic Resonances in Self-Assembled Reduced Symmetry Gold Nanorod Structures. *Nano Lett.* **2013**, *13*, 2220−2225.

(60) Nazir, A.; Panaro, S.; Proietti Zaccaria, R.; Liberale, C.; De Angelis, F.; Toma, A. Fano Coil-Type Resonance for Magnetic Hot-Spot Generation. *Nano Lett.* **2014**, *14*, 3166−3171.

(61) Verellen, N.; Lopez-Tejeira, F.; Paniagua-Dominguez, R.; Vercruysse, D.; Denkova, D.; Lagae, L.; Van Dorpe, P.; Moshchalkov, V. V.; Sanchez-Gil, J. A. Mode Parity-Controlled Fano- and Lorentz-Like Line Shapes Arising in Plasmonic Nanorods. *Nano Lett.* **2014**, *14*, 2322−2329.

(62) Brown, L. V.; Sobhani, H.; Lassiter, J. B.; Nordlander, P.; Halas, N. J. Heterodimers: Plasmonic Properties of Mismatched Nanoparticle Pairs. *ACS Nano* **2010**, *4*, 819−832.

(63) Fan, J. A.; Bao, K.; Wu, C.; Bao, J.; Bardhan, R.; Halas, N. J.; Manoharan, V. N.; Shvets, G.; Nordlander, P.; Capasso, F. Fano-Like Interference in Self-Assembled Plasmonic Quadrumer Clusters. *Nano Lett.* **2010**, *10*, 4680−4685.

(64) Frontiera, R. R.; Gruenke, N. L.; Van Duyne, R. P. Fano-Like Resonances Arising from Long-Lived Molecule-Plasmon Interactions in Colloidal Nanoantennas. *Nano Lett.* **2012**, *12*, 5989−5994.

(65) Stiles, P. L.; Dieringer, J. A.; Shah, N. C.; Van Duyne, R. R. Surface-Enhanced Raman Spectroscopy. *Annu. Rev. Anal. Chem.* **2008**, *1*, 601−626.

(66) Tcherniak, A.; Ha, J. W.; Dominguez-Medina, S.; Slaughter, L. S.; Link, S. Probing a Century Old Prediction One Plasmonic Particle at a Time. *Nano Lett.* **2010**, *10*, 1398−1404.

(67) Chang, W. S.; Willingham, B.; Slaughter, L. S.; Dominguez-Medina, S.; Swanglap, P.; Link, S. Radiative and Nonradiative Properties of Single Plasmonic Nanoparticles and Their Assemblies. *Acc. Chem. Res.* **2012**, *45*, 1936−1945.

(68) Schwartzberg, A. M.; Zhang, J. Z. Novel Optical Properties and Emerging Applications of Metal Nanostructures. *J. Phys. Chem. C* **2008**, *112*, 10323−10337.

(69) Stranahan, S. M.; Titus, E. J.; Willets, K. A. Sers Orientational Imaging of Silver Nanoparticle Dimers. *J. Phys. Chem. Lett.* **2011**, *2*, 2711−2715.

(70) Stranahan, S. M.; Titus, E. J.; Willets, K. A. Discriminating Nanoparticle Dimers from Higher Order Aggregates through Wavelength-Dependent Sers Orientational Imaging. *ACS Nano* **2012**, *6*, 1806−1813.

(71) Willets, K. A.; Van Duyne, R. P. Localized Surface Plasmon Resonance Spectroscopy and Sensing. *Annu. Rev. Phys. Chem.* **2007**, *58*, 267−297.

(72) Anker, J. N.; Hall, W. P.; Lyandres, O.; Shah, N. C.; Zhao, J.; Van Duyne, R. P. Biosensing with Plasmonic Nanosensors. *Nat. Mater.* **2008**, *7*, 442−453.

(73) Jiang, N.; Foley, E. T.; Klingsporn, J. M.; Sonntag, M. D.; Valley, N. A.; Dieringer, J. A.; Seideman, T.; Schatz, G. C.; Hersam, M. C.; Van Duyne, R. P. Observation of Multiple Vibrational Modes in Ultrahigh Vacuum Tip-Enhanced Raman Spectroscopy Combined with Molecular-Resolution Scanning Tunneling Microscopy. *Nano Lett.* **2012**, *12*, 5061−5067.

(74) Sivapalan, S. T.; DeVetter, B. M.; Yang, T. K.; van Dijk, T.; Schulmerich, M. V.; Carney, P. S.; Bhargava, R.; Murphy, C. J. Off-Resonance Surface-Enhanced Raman Spectroscopy from Gold Nanorod Suspensions as a Function of Aspect Ratio: Not What We Thought. *ACS Nano* **2013**, *7*, 2099−2105.

(75) Wang, H.; Schultz, Z. D. The Chemical Origin of Enhanced Signals from Tip-Enhanced Raman Detection of Functionalized Nanoparticles. *Analyst* **2013**, *138*, 3150−3157.

(76) Zhang, Y.; Zhen, Y. R.; Neumann, O.; Day, J. K.; Nordlander, P.; Halas, N. J. Coherent Anti-Stokes Raman Scattering with Single-Molecule Sensitivity Using a Plasmonic Fano Resonance. *Nat. Commun.* **2014**, *5*, 7.

(77) Sonntag, M. D.; Klingsporn, J. M.; Zrimsek, A. B.; Sharma, B.; Ruvuna, L. K.; Van Duyne, R. P. Molecular Plasmonics for Nanoscale Spectroscopy. *Chem. Soc. Rev.* **2014**, *43*, 1230−1247.

(78) Henry, A. I.; Bingham, J. M.; Ringe, E.; Marks, L. D.; Schatz, G. C.; Van Duyne, R. P. Correlated Structure and Optical Property Studies of Plasmonic Nanoparticles. *J. Phys. Chem. C* **2011**, *115*, 9291−9305.

(79) Nie, S. M.; Emery, S. R. Probing Single Molecules and Single Nanoparticles by Surface-Enhanced Raman Scattering. *Science* **1997**, *275*, 1102−1106.

(80) Kneipp, K.; Wang, Y.; Kneipp, H.; Perelman, L. T.; Itzkan, I.; Dasari, R.; Feld, M. S. Single Molecule Detection Using Surface-Enhanced Raman Scattering (Sers). *Phys. Rev. Lett.* **1997**, *78*, 1667−1670.

(81) Michaels, A. M.; Nirmal, M.; Brus, L. E. Surface Enhanced Raman Spectroscopy of Individual Rhodamine 6g Molecules on Large Ag Nanocrystals. *J. Am. Chem. Soc.* **1999**, *121*, 9932−9939.

(82) Xu, H. X.; Bjerneld, E. J.; Kall, M.; Borjesson, L. Spectroscopy of Single Hemoglobin Molecules by Surface Enhanced Raman Scattering. *Phys. Rev. Lett.* **1999**, *83*, 4357−4360.

(83) Titus, E. J.; Willets, K. A. Superlocalization Surface-Enhanced Raman Scattering Microscopy: Comparing Point Spread Function Models in the Ensemble and Single-Molecule Limits. *ACS Nano* **2013**, *7*, 8284−8294.

(84) Titus, E. J.; Willets, K. A. Accuracy of Superlocalization Imaging Using Gaussian and Dipole Emission Point-Spread Functions for Modeling Gold Nanorod Luminescence. *ACS Nano* **2013**, *7*, 6258−6267.

(85) Willets, K. A. New Tools for Investigating Electromagnetic Hot Spots in Single-Molecule Surface-Enhanced Raman Scattering. *ChemPhysChem* **2013**, *14*, 3186−3195.

(86) Willets, K. A. Super-Resolution Imaging of Sers Hot Spots. *Chem. Soc. Rev.* **2014**, *43*, 3854−3864.

(87) Zhou, X. C.; Andoy, N. M.; Liu, G. K.; Choudhary, E.; Han, K. S.; Shen, H.; Chen, P. Quantitative Super-Resolution Imaging Uncovers Reactivity Patterns on Single Nanocatalysts. *Nat. Nanotechnol.* **2012**, *7*, 237−241.

(88) Biswas, S.; Liu, X.; Jarrett, J. W.; Brown, D.; Pustovit, V.; Urbas, A.; Knappenberger, K. L., Jr.; Nealey, P. F.; Vaia, R. Nonlinear Chiro-Optical Amplification of Plasmonic Nanolens Arrays Formed Via Directed Assembly of Gold Nanoparticles. *Nano Lett.* **2015**, *15*, 1836−1842.

(89) Feldstein, M. J.; Vohringer, P.; Wang, W.; Scherer, N. F. Femtosecond Optical Spectroscopy and Scanning Probe Microscopy. *J. Phys. Chem.* **1996**, *100*, 4739−4748.

(90) Liau, Y. H.; Unterreiner, A. N.; Chang, Q.; Scherer, N. F. Ultrafast Dephasing of Single Nanoparticles Studied by Two-Pulse Second-Order Interferometry. *J. Phys. Chem. B* **2001**, *105*, 2135−2142.

(91) Kubo, A.; Onda, K.; Petek, H.; Sun, Z. J.; Jung, Y. S.; Kim, H. K. Femtosecond Imaging of Surface Plasmon Dynamics in a Nanostructured Silver Film. *Nano Lett.* **2005**, *5*, 1123−1127.

(92) van Dijk, M. A.; Lippitz, M.; Orrit, M. Detection of Acoustic Oscillations of Single Gold Nanospheres by Time-Resolved Interferometry. *Phys. Rev. Lett.* **2005**, *95*, 267406.

(93) Pelton, M.; Liu, M. Z.; Park, S.; Scherer, N. F.; Guyot-Sionnest, P. Ultrafast Resonant Optical Scattering from Single Gold Nanorods: Large Nonlinearities and Plasmon Saturation. *Phys. Rev. B* **2006**, *73*, 6.

(94) Kubo, A.; Pontius, N.; Petek, H. Femtosecond Microscopy of Surface Plasmon Polariton Wave Packet Evolution at the Silver/Vacuum Interface. *Nano Lett.* **2007**, *7*, 470−475.

(95) Park, S.; Pelton, M.; Liu, M.; Guyot-Sionnest, P.; Scherer, N. F. Ultrafast Resonant Dynamics of Surface Plasmons in Gold Nanorods. *J. Phys. Chem. C* **2007**, *111*, 116−123.

(96) van Dijk, M. A.; Lippitz, M.; Stolwijk, D.; Orrit, M. A Common-Path Interferometer for Time-Resolved and Shot-Noise-Limited Detection of Single Nanoparticles. *Opt. Express* **2007**, *15*, 2273−2287.

(97) Staleva, H.; Hartland, G. V. Vibrational Dynamics of Silver Nanocubes and Nanowires Studied by Single-Particle Transient Absorption Spectroscopy. *Adv. Funct. Mater.* **2008**, *18*, 3809−3817.

(98) Staleva, H.; Hartland, G. V. Transient Absorption Studies of Single Silver Nanocubes. *J. Phys. Chem. C* **2008**, *112*, 7535−7539.

(99) Zijlstra, P.; Tchebotareva, A. L.; Chon, J. W. M.; Gu, M.; Orrit, M. Acoustic Oscillations and Elastic Moduli of Single Gold Nanorods. *Nano Lett.* **2008**, *8*, 3493−3497.

(100) Aeschlimann, M.; Brixner, T.; Fischer, A.; Kramer, C.; Melchior, P.; Pfeiffer, W.; Schneider, C.; Struber, C.; Tuchscherer, P.; Voronine, D. V. Coherent Two-Dimensional Nanoscopy. *Science* **2011**, *333*, 1723−1726.

(101) Grubisic, A.; Ringe, E.; Cobley, C. M.; Xia, Y.; Marks, L. D.; Van Duyne, R. P.; Nesbitt, D. J. Plasmonic near-Electric Field Enhancement Effects in Ultrafast Photoelectron Emission: Correlated Spatial and Laser Polarization Microscopy Studies of Individual Ag Nanocubes. *Nano Lett.* **2012**, *12*, 4823−4829.

(102) Lo, S. S.; Shi, H. Y.; Huang, L. B.; Hartland, G. V. Imaging the Extent of Plasmon Excitation in Au Nanowires Using Pump-Probe Microscopy. *Opt. Lett.* **2013**, *38*, 1265−1267.

(103) Shah, R. A.; Scherer, N. F.; Pelton, M.; Gray, S. K. Ultrafast Reversal of a Fano Resonance in a Plasmon-Exciton System. *Phys. Rev. B* **2013**, *88*, 7.

(104) Accanto, N.; Piatkowski, L.; Renger, J.; van Hulst, N. F. Capturing the Optical Phase Response of Nanoantennas by Coherent Second-Harmonic Microscopy. *Nano Lett.* **2014**, *14*, 4078−4082.

(105) Major, T. A.; Devadas, M. S.; Lo, S. S.; Hartland, G. V. Optical and Dynamical Properties of Chemically Synthesized Gold Nanoplates. *J. Phys. Chem. C* **2013**, *117*, 1447−1452.

(106) Zijlstra, P.; Paulo, P. M. R.; Yu, K.; Xu, Q. H.; Orrit, M. Chemical Interface Damping in Single Gold Nanorods and Its Near

Elimination by Tip-Specific Functionalization. *Angew. Chem., Int. Ed.* **2012**, *51*, 8352−8355.

(107) Zijlstra, P.; Paulo, P. M. R.; Orrit, M. Optical Detection of Single Non-Absorbing Molecules Using the Surface Plasmon Resonance of a Gold Nanorod. *Nat. Nanotechnol.* **2012**, *7*, 379−382.

(108) Masia, F.; Langbein, W.; Borri, P. Measurement of the Dynamics of Plasmons inside Individual Gold Nanoparticles Using a Femtosecond Phase-Resolved Microscope. *Phys. Rev. B* **2012**, *85*.

(109) Anderson, A.; Deryckx, K. S.; Xu, X. J. G.; Steinmeyer, G.; Raschke, M. B. Few-Femtosecond Plasmon Dephasing of a Single Metallic Nanostructure from Optical Response Function Reconstruction by Interferometric Frequency Resolved Optical Gating. *Nano Lett.* **2010**, *10*, 2519−2524.

(110) Sonnichsen, C.; Franzl, T.; Wilk, T.; von Plessen, G.; Feldmann, J.; Wilson, O.; Mulvaney, P. Drastic Reduction of Plasmon Damping in Gold Nanorods. *Phys. Rev. Lett.* **2002**, *88*.

(111) Hu, M.; Novo, C.; Funston, A.; Wang, H.; Staleva, H.; Zou, S.; Mulvaney, P.; Xia, Y.; Hartland, G. V. Dark-Field Microscopy Studies of Single Metal Nanoparticles: Understanding the Factors That Influence the Linewidth of the Localized Surface Plasmon Resonance. *J. Mater. Chem.* **2008**, *18*, 1949−1960.

(112) Hartland, G. V. Optical Studies of Dynamics in Noble Metal Nanostructures. *Chem. Rev. (Washington, DC, U.S.)* **2011**, *111*, 3858−3887.

(113) Jarrett, J. W.; Chandra, M.; Knappenberger, K. L., Jr. Optimization of Nonlinear Optical Localization Using Electromagnetic Surface Fields (Noles) Imaging. *J. Chem. Phys.* **2013**, *138*, 214202.

(114) Rehault, J.; Maiuri, M.; Manzoni, C.; Brida, D.; Helbing, J.; Cerullo, G. 2d Ir Spectroscopy with Phase-Locked Pulse Pairs from a Birefringent Delay Line. *Opt. Express* **2014**, *22*, 9063−9072.

(115) Rehault, J.; Maiuri, M.; Oriana, A.; Cerullo, G. Two-Dimensional Electronic Spectroscopy with Birefringent Wedges. *Rev. Sci. Instrum.* **2014**, *85*, 10.

(116) Jarrett, J. W.; Liu, X.; Nealey, P. F.; Vaia, R.; Cerullo, G.; Knappenberger, K. L., Jr. SHG-Detected Circular Dichroism Imaging Using Orthogonal Phase-Locked Laser Pulses. *J. Chem. Phys.* **2015**, *142*, 151101.

(117) Thompson, R. E.; Larson, D. R.; Webb, W. W. Precise Nanometer Localization Analysis for Individual Fluorescent Probes. *Biophys. J.* **2002**, *82*, 2775−2783.

(118) Mazziotta, M. N. Electron−Hole Pair Creation Energy and Fano Factor Temperature Dependence in Silicon. *Nucl. Instrum. Methods Phys. Res., Sect. A* **2008**, *584*, 436−439.

(119) Enderlein, J.; Toprak, E.; Selvin, P. R. Polarization Effect on Position Accuracy of Fluorophore Localization. *Opt. Express* **2006**, *14*, 8111−8120.

(120) Wu, X. L.; Xu, L. G.; Liu, L. Q.; Ma, W.; Yin, H. H.; Kuang, H.; Wang, L. B.; Xu, C. L.; Kotov, N. A. Unexpected Chirality of Nanoparticle Dimers and Ultrasensitive Chiroplasmonic Bioanalysis. *J. Am. Chem. Soc.* **2013**, *135*, 18629−18636.

(121) Tian, X. R.; Fang, Y. R.; Zhang, B. L. Multipolar Fano Resonances and Fano-Assisted Optical Activity in Silver Nanorice Heterodimers. *ACS Photonics* **2014**, *1*, 1156−1164.

(122) Fan, Z.; Zhang, H.; Govorov, A. O. Optical Properties of Chiral Plasmonic Tetramers: Circular Dichroism and Multipole Effects. *J. Phys. Chem. C* **2013**, *117*, 14770−14777.

(123) Kauranen, M.; Verbiest, T.; Maki, J. J.; Persoons, A. 2nd-Harmonic Generation from Chiral Surfaces. *J. Chem. Phys.* **1994**, *101*, 8193−8199.

(124) Hoggard, A.; Wang, L. Y.; Ma, L. L.; Fang, Y.; You, G.; Olson, J.; Liu, Z.; Chang, W. S.; Ajayan, P. M.; Link, S. Using the Plasmon Linewidth to Calculate the Time and Efficiency of Electron Transfer Between Gold Nanorods and Graphene. *ACS Nano* **2013**, *7*, 11209−11217.

(125) Trebino, R. *Frequency-Resolved Optical Gating: The Measurement of Ultrashort Laser Pulses: The Measurement of Ultrashort Laser Pulses*; Springer: New York, 2000.

(126) Fang, Y.; Chang, W. S.; Willingham, B.; Swanglap, P.; Dominguez-Medina, S.; Link, S. Plasmon Emission Quantum Yield of

Single Gold Nanorods as a Function of Aspect Ratio. *ACS Nano* **2012**, 6, 7177−7184.

(127) Hu, H. L.; Duan, H. G.; Yang, J. K. W.; Shen, Z. X. Plasmon-Modulated Photoluminescence of Individual Gold Nanostructures. *ACS Nano* **2012**, 6, 10147−10155.

(128) Chen, W. L.; Lin, F. C.; Lee, Y. Y.; Li, F. C.; Chang, Y. M.; Huang, J. S. The Modulation Effect of Transverse, Antibonding, and Higher-Order Longitudinal Modes on the Two-Photon Photoluminescence of Gold Plasmonic Nanoantennas. *ACS Nano* **2014**, 8, 9053−9062.

(129) Konar, A.; Shah, J. D.; Lozovoy, V. V.; Dantus, M. Optical Response of Fluorescent Molecules Studied by Synthetic Femtosecond Laser Pulses. *J. Phys. Chem. Lett.* **2012**, 3, 1329−1335.

(130) Scholes, G. D. Long-Range Resonance Energy Transfer in Molecular Systems. *Annu. Rev. Phys. Chem.* **2003**, 54, 57−87.

(131) Song, C.; Blaber, M. G.; Zhao, G.; Zhang, P.; Fry, H. C.; Schatz, G. C.; Rosi, N. L. Tailorable Plasmonic Circular Dichroism Properties of Helical Nanoparticle Superstructures. *Nano Lett.* **2013**, 13, 3256−3261.

(132) Acevedo, R.; Lombardini, R.; Halas, N. J.; Johnson, B. R. Plasmonic Enhancement of Raman Optical Activity in Molecules near Metal Nanoshells. *J. Phys. Chem. A* **2009**, 113, 13173−13183.

(133) Govorov, A. O.; Fan, Z.; Hernandez, P.; Slocik, J. M.; Naik, R. R. Theory of Circular Dichroism of Nanomaterials Comprising Chiral Molecules and Nanocrystals: Plasmon Enhancement, Dipole Interactions, and Dielectric Effects. *Nano Lett.* **2010**, 10, 1374−1382.

(134) Lombardini, R.; Acevedo, R.; Halas, N. J.; Johnson, B. R. Plasmonic Enhancement of Raman Optical Activity in Molecules near Metal Nanoshells: Theoretical Comparison of Circular Polarization Methods. *J. Phys. Chem. C* **2010**, 114, 7390−7400.

(135) Layani, M. E.; Ben Moshe, A.; Varenik, M.; Regev, O.; Zhang, H.; Govorov, A. O.; Markovich, G. Chiroptical Activity in Silver Cholate Nanostructures Induced by the Formation of Nanoparticle Assemblies. *J. Phys. Chem. C* **2013**, 117, 22240−22244.

(136) Maoz, B. M.; Chaikin, Y.; Tesler, A. B.; Bar Elli, O.; Fan, Z.; Govorov, A. O.; Markovich, G. Amplification of Chiroptical Activity of Chiral Biomolecules by Surface Plasmons. *Nano Lett.* **2013**, 13, 1203−1209.

(137) Keiderling, T. A. Observation of Magnetic Vibrational Circular-Dichroism. *J. Chem. Phys.* **1981**, 75, 3639−3641.

(138) Wong, N. C.; Kintzer, E. S.; Mlynek, J.; Devoe, R. G.; Brewer, R. G. Raman Heterodyne-Detection of Nuclear Magnetic-Resonance. *Phys. Rev. B* **1983**, 28, 4993−5010.

(139) Holliday, K.; He, X. F.; Fisk, P. T. H.; Manson, N. B. Raman Heterodyne-Detection of Electron-Paramagnetic Resonance. *Opt. Lett.* **1990**, 15, 983−985.

(140) Bingham, S. J.; Rasmussen, T.; Farrar, J.; Wolverson, D.; Thomson, A. J. Magnetic Circular Dichroism Anisotropy of the Cu-a Centre of Nitrous Oxide Reductase from Coherent Raman Detected Electron Spin Resonance Spectroscopy. *Mol. Phys.* **2007**, 105, 2169−2176.

(141) Bingham, S. J.; Wolverson, D.; Thomson, A. J. Coherent Raman Detected Electron Spin Resonance Spectroscopy of Metalloproteins: Linking Electron Spin Resonance and Magnetic Circular Dichroism. *Biochem. Soc. Trans.* **2008**, 36, 1187−1190.